

**Preparation and characterisation of
 $\text{Fe}_3\text{O}_4/\text{MgO}/\text{Fe}$ and $\text{Fe}_3\text{O}_4/\text{MgO}/\text{Cr}$ thin film stacks**

A thesis submitted to the University of Dublin, Trinity College in
application for the degree of Master of Science

By

Ciarán McEvoy

School of Physics
Trinity College Dublin

January 2006

Declaration:

This thesis is submitted by the undersigned for the degree of Master of Science at the University of Dublin.

It has not been submitted as an exercise for a degree at any other university.

Apart from the advice, assistance and joint effort mentioned in the acknowledgements and in the text, this thesis is all my own work.

I agree that the library may lend or copy this thesis freely on request.

Ciarán McEvoy

Acknowledgements:

Firstly I would like to thank Prof. Igor Shvets for affording me the opportunity, and providing me with the resources, to pursue this research in the Nanomag group. I would also like to thank the Department of Physics, as it was when I began, for opening its doors to me.

Secondly I would like to thank our group administrator, Marie Kinsella, for all her good humoured assistance throughout my stay here in Trinity. It fell to her to sort out all the thankless official tasks. For this I thank her.

Most importantly I would like to thank my direct supervisor, Xuesong Jin. Without him I would not have been able to complete this research and would still be scratching my head wondering what it is I should be doing. I have never had the privilege to meet a person more generous with their time and knowledge. I cannot even come close to remembering how many times he helped me with suggestions or his technical expertise. All of this was done in the best humour imaginable, even when I was getting stressed and grumpy. I can not thank him enough for all his help.

I would also like to thank all the technical staff of the department. In particular I would like to thank Mick Reilly and Dave Grouse of the mechanical work shop for all their help in fabricating numerous sample holders and other mechanical gizmos, as well as their help with both liquid nitrogen and helium. No matter how sketchy my drawings they managed to interpret them and produce the correct piece, God knows how. I would also like to thank Ken Concannon for all his computer related help. Without him my PC would be riddled with viruses and everything lost.

Now I would like to thank all the members of the Nanomag group. In particular I would like to thank my fellow students of the Thin Film side of the group, Sumesh, Rafa and Floriano. As much as it was possible, it was a pleasure to share the hot and sticky days in the MBE lab with them. On the whole, the group proved to be a very welcoming bunch and were not

indisposed to part-taking in the odd beverage when the time was right. For all the good times, of which there were many, thank you.

Lastly I would like to thank my family and friends for being there when things were getting a little much. I would very much like to thank my dad for all his support when I decided to quit my job and return to study. I want to say a big thank you also to my two sisters for many memorable moments of light relief and being there when things weren't going quite to plan. Lastly a huge thanks to Ilona for all her support and love during my time here in Trinity, even though she was snowed under with her own study. Throughout the good times and the bad she was there to make things better and helped me through the bad times after the death of my father. For this and everything I say thank you and love always.

Abstract:

Two similar epitaxial thin film stack structures, grown by oxygen plasma assisted molecular beam epitaxy, were investigated to determine the influence the barrier layer had on the properties of the stack.

Firstly the growth and interface roughness correlation in heteroepitaxial $\text{Fe}_3\text{O}_4/\text{MgO}/\text{Fe}$ stacks grown on single crystal MgO (100) substrates was investigated. Evidence for the correlation of layer interface roughness was found when the thickness of the MgO barrier layer was less than 1 nm but not when the barrier layer was thicker than 2 nm. This was attributed to a thickness dependent change in the growth mode. The 1 nm layer was predicted to grow in the 2D mode while at greater thickness the growth mode changed to 3D, thus destroying the interface roughness correlation. Our results indicate that the thickness dependent interface roughness correlation may have a role to play on the electrical properties of the magnetic tunnel junction. Our research demonstrates that MgO barrier layers of thickness less than 1 nm may be suitable for use in magnetic tunnel junctions.

The second system investigated was a (30 nm) Fe_3O_4 (100) / (1 – 6 nm) MgO (100) / (5 nm) Cr (100) and a (5 nm) MgO (100) / (5 nm) Cr structure, both deposited on MgO (100) substrate. The proximity influence of the bottom magnetite electrode on the in-plane transport and magnetotransport properties of the structures was investigated. A reversal of the magnetoresistance (MR) sign for the Cr layer was observed when the MgO barrier layer was less than 5 nm thick. The thickness of the MgO layer through which the influence of the magnetite bottom electrode on the top Cr film was felt was too large to be explained by an exchange interaction. The results suggest that the magnetic structure in the Cr film adjoining a pinhole in the MgO layer is distorted due to exchange coupling. Such areas in the Cr film are thought to contribute to the negative MR.

Publications:

Xuesong Jin, Ciarán McEvoy, I. V. Shvets, “Studies of heteroepitaxial growth of Fe/MgO/Fe₃O₄ multilayer on MgO (100) substrates for the fabrication of magnetic tunnel junctions”, J. Magn. Magn. Mater., **286** (2005) 128

Ciarán McEvoy, Xuesong Jin, I. V. Shvets, “Proximity influence of a ferromagnet on the magnetoresistance of Cr film across a nonmagnetic layer”, J. Magn. Magn. Mater. **283** (2004) 171

List of Figures:

Figure 1.1	Schematic of a basic Magnetic Tunnel Junction	2
Figure 1.2	Schematic of a magnetoresistive read sensor passing over regions magnetised in opposite direction	3
Figure 1.3	Schematic illustration of a magnetic random access memory	4
Figure 2.1	Schematic of the Fe_3O_4 unit cell	7
Figure 2.2	Schematic representation of the band structure of magnetite	8
Figure 2.3	Schematic of the MgO lattice, showing its rock-salt structure	9
Figure 2.4	Schematic representation of the magnetisation orientation dependent resistance in a magnetic tunnel junction	11
Figure 2.5	Schematic of a Ewald sphere	15
Figure 2.6	Ewald sphere construction and diffraction geometry of RHEED	17
Figure 2.7	Schematic of a fully strained substrate – film system	18
Figure 2.8	X-Ray diffraction geometry configurations	21
Figure 3.1	Photograph of the MBE system	23
Figure 3.2	Schematic of the MBE system	27
Figure 3.3	Schematic of the RHEED system configuration	33
Figure 3.4	Schematic of the Bede D1 X-Ray diffractometer layout	36
Figure 3.5	Photograph of the Bede D1 X-Ray diffractometer layout	36
Figure 3.6	Schematic of the CCR Resistivity Measurement system	39
Figure 3.7	Photograph of the CCR Resistivity Measurement cold head	40
Figure 3.8	Schematic of the CCR Resistivity Measurement system	41
Figure 3.9	Schematic of the Mo substrate holder	43
Figure 4.1	X-Ray diffraction rocking curve for the symmetric (004) peak of the Fe_3O_4 film	47
Figure 4.2	Reciprocal space map near the asymmetric (226) glancing exit diffraction of the Fe_3O_4 film	47
Figure 4.3	Resistivity of the Fe_3O_4 film as a function of temperature	48
Figure 4.4	RHEED images of the growth of the $\text{Fe}_3\text{O}_4/\text{MgO}/\text{Fe}/\text{MgO}$ epitaxial thin film stack structure	49

Figure 4.5	Spectral X-Ray reflectivity of the $\text{Fe}_3\text{O}_4/\text{MgO}/\text{Fe}/\text{MgO}$ epitaxial thin film stack	51
Figure 4.6	X-Ray reflectivity reciprocal space map for sample 1 and sample 2 of the $\text{Fe}_3\text{O}_4/\text{MgO}/\text{Fe}/\text{MgO}$ epitaxial thin film stack	52
Figure 5.1	RHEED images of the growth of the $\text{Fe}_3\text{O}_4/\text{MgO}/\text{Cr}/\text{MgO}/$ epitaxial thin film stack structure	57
Figure 5.2	X-Ray diffraction rocking curve for the symmetric (004) and asymmetric (226) peaks of a 30 nm thick magnetite film	58
Figure 5.3	Resistivity and magnetoresistivity at 1500 kA/m of a 30 nm thick magnetite film as a function of temperature	60
Figure 5.4	Resistivity and magnetoresistivity at 1500 kA/m of a 5 nm thick Cr film as a function of temperature	60
Figure 5.5	Dependence of the magnetoresistance of the $\text{Fe}_3\text{O}_4/\text{MgO}/\text{Cr}/\text{MgO}$ structure at field strength of 1500 kA/m and a temperature of 30 K	61
Figure 5.6	Calculated magnetoresistance of the Cr film – Fe_3O_4 electrode system as a function of the film to substrate resistance ratio	63
Figure 5.7	X-Ray reflectivity reciprocal space map for the $\text{Fe}_3\text{O}_4/\text{MgO}/\text{Cr}/\text{MgO}$ structure	65
Figure 5.8	Schematic of the distorted magnetic configuration in the $\text{Fe}_3\text{O}_4/\text{MgO}/\text{Cr}/\text{MgO}$ system to explain the observed results	67

List of tables:

Table 3.1	Description of the XRD measurements performed during the course of the research	38
Table 4.1	Roughness derived from the specular reflectivity curve for the Fe ₃ O ₄ /MgO/Fe/MgO epitaxial thin film stack structure	51
Table 5.1	Calculated coupling field based on the “orange peel” model for the Fe ₃ O ₄ /MgO/Cr/ MgO epitaxial thin film stack structure	64

Contents:

1	Introduction	1
1.1	Introduction	1
1.2	Discovery of Tunnelling Magnetoresistance (TMR)	1
1.3	Devices	2
1.4	Motivation	4
2	Theoretical Considerations	7
2.1	Properties of Magnetite	7
2.2	Fe ₃ O ₄ – MgO Lattice Mis-match	9
2.3	Properties of Thin Epitaxial Cr Layer	10
2.4	Tunnelling Magnetoresistance	10
2.5	Reflection High Energy Electron Diffraction (RHEED) Theory	15
2.6	High Resolution X-Ray Diffraction (HRXRD)	
	Lattice Parameter Calculations	18
3	Experimental Details	22
3.1	Introduction	22
3.2	Molecular Beam Epitaxy (MBE) System	22
3.2.1	Load-Lock Chamber	23
3.2.2	Deposition Chamber	24
3.2.3	Substrate Manipulator	28
3.2.4	Water Cooling System	29
3.2.5	Interlock System	30
3.2.6	Reflection High Energy Electron Diffraction (RHEED)	31
3.2.7	Plasma Source	33
3.3	High Resolution X-Ray Diffractometer	34
3.4	Closed Cycle Refrigeration (CCR) System	38
3.5	Sample Preparation and Loading	41

4	The Fe ₃ O ₄ /MgO/Fe Epitaxial Thin Film Stack	44
4.1	Introduction	44
4.2	Structural Growth and Characterisation	45
4.3	Experimental Results and Discussion	46
4.4	Conclusion	53
5	The Fe ₃ O ₄ /MgO/Cr Epitaxial Thin Film Stack	54
5.1	Introduction	54
5.2	Structural Growth and Characterisation	55
5.3	Experimental Results	56
5.4	Discussion	61
5.4.1	Electrical Bridging Through the Pinholes	62
5.4.2	Magnetostatic ("Orange Peel") Coupling	63
5.4.3	Direct Magnetic Coupling through the Pinholes	65
5.5	Conclusion	68
6	Conclusion	69
7	Bibliography	71

Chapter 1: Introduction

1.1 Introduction

This thesis will focus on the role of the insulating layer, also referred to as the barrier layer, on the operation of a magnetic tunnel junction (MTJ). The notion of a MTJ has its origins when the non-magnetic layer of a Giant Magnetoresistance (GMR) structure was replaced with an insulating layer. Thus a MTJ is generally referred to using the following notation, FM-I-FM, where FM refers to the ferromagnetic electrode and I refers to the insulating layer. The two structures differ in the magnetic coupling between the electrodes. In a GMR structure there is ferromagnetic coupling between the electrodes while in a MTJ structure the coupling between the electrodes is antiferromagnetic.

At the heart of the operation of a MTJ is the notion of spin polarisation of the transport current due to spin dependent scattering. This is denoted Spin Polarised Tunnelling (SPT). Ferromagnetic metals are used in MTJs because they possess a spontaneous magnetisation due to the spin imbalance in the density of the d-state electrons. A fraction of these spin polarised electrons, referred to as the itinerant d-electrons, contribute to the tunnelling current, as do the un-paired s- and p-electrons. This implies that the current is partially spin polarised. In a MTJ the current is mainly due to the itinerant d-electrons.

1.2 Discovery of Tunnelling Magnetoresistance (TMR)

The first reported magnetoresistance (MR) measurements made on a FM-I-FM trilayer junction were published by Julliere [1]. A schematic of a simple FM-I-FM trilayer is given in figure 1.1 below (it is the most basic representation of a magnetic tunnel junction). His experiment was based on the property of spin polarised tunnelling (SPT) initially discovered by Meservey *et al* [2] and Meservey and Tedrow [3, 4]. Meservey and Tedrow measured the conduction electron spin polarisation in magnetic metals and compounds using the Zeeman split quasiparticle density of states in a superconductor as the spin detector. Tunnelling from a FM electrode, with its uneven spin distribution at the Fermi level (E_F), into a spin split superconducting film reflected the spin polarisation of the tunnelling electrons coming from the ferromagnet.

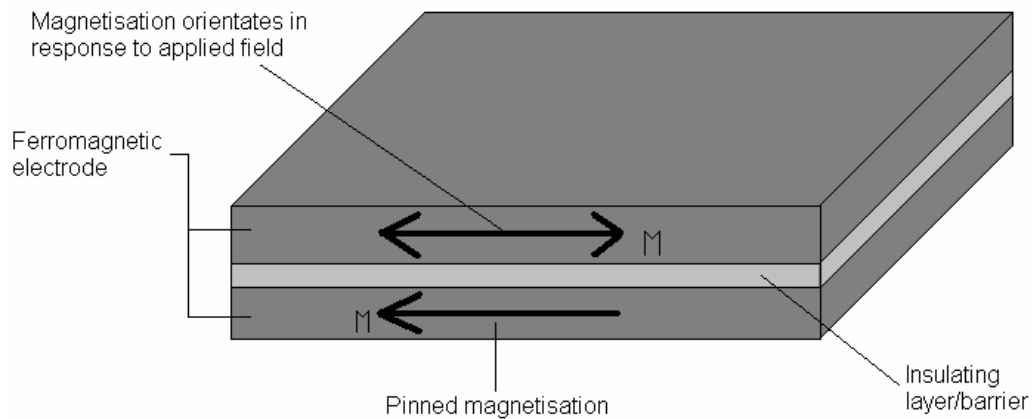


Figure 1.1: Schematic of the most basic magnetic tunnel junction (a FM-I-FM trilayer)

Julliere referred to the MR measurements he made as Tunnelling Magnetoresistance (TMR). For his measurements he employed a TMR sandwich in which a thin insulating layer of Ge separated a thin Fe layer from a thin Co layer. The thickness of the Ge layer was chosen to minimise the magnetic coupling between the two FM layers. The FM layers had a common easy axis of magnetisation but different coercivities. Julliere proposed that the TMR observed was determined by the relative orientation of the magnetisation of the two FM layers. He proposed that when the magnetic field strength (H) lay between the two coercive fields the magnetisations of the FM electrodes were aligned anti-parallel to each other. This anti-parallel alignment between the two electrodes caused an increase in the spin scattering and as such a reduction in the conductivity was observed. When the magnetic field strength was increased sufficiently, in excess of the coercive fields of both FM electrodes, the magnetisations were aligned parallel. In this parallel configuration an increase in the conductivity was observed, and conversely a decrease in the resistivity was observed. This will be covered in more details in the Theoretical Consideration section.

1.3 Devices

In today's society there is an increasing demand for information and a means to store it in a digital format. Presently data is stored digitally by means of μm sized "bits" within magnetic

layers or disks. The size of the magnetic bits determines the capacity of the storage medium. Magnetic tunnel junctions (MTJ) can be used as read sensors to measure stray magnetic fields from each bit and convert it into an electrical signal. A schematic of a magnetoresistive read sensor is shown in figure 1.2 below [5]. As shown, the perpendicular stray fields from the media cause an anti-parallel alignment of the magnetisations of the magnetic layers in the read head. This causes a change in the current passing through the sensor caused by the magnetisation alignment induced change in resistance.

Magnetic tunnel junctions are also candidates for advanced non-volatile magnetic random access memory (MRAM). A schematic of such a device is shown in figure 1.3 below [5]. In such a MRAM the MTJ is integrated at each crossing between a “word” and a “sense” line. The “word” and the “sense” lines have a double role. They act to measure the resistance of the junction and they also create the magnetic fields required to switch the resistance of the junction.

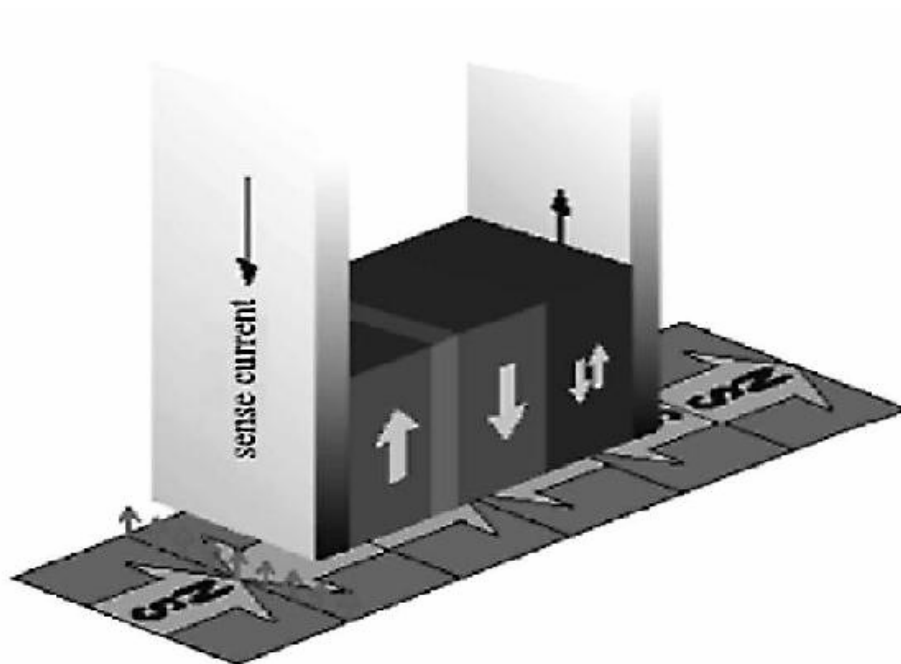


Figure 1.2: Schematic of a magnetoresistive read sensor passing over regions magnetised in opposite directions.

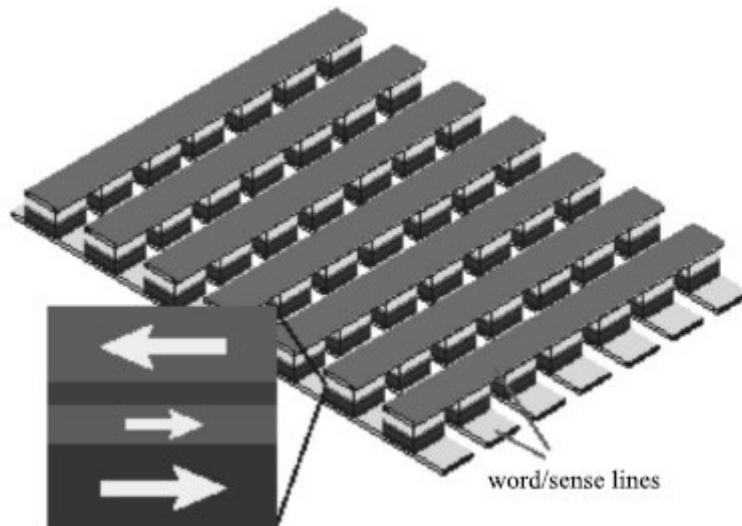


Figure 1.3: Schematic illustration of a magnetic random access memory

1.4 Motivation

Spin-dependent tunnelling between two ferromagnetic (FM) films across an insulator has significant potential for applications in digital storage devices and magnetic sensor technologies [6 - 9]. Previously, Magnetoresistance (MR) greater than 20% has been reported in spin tunnel junctions at room temperature [10 – 12]. However, more recently Parkin *et al* [13] and Yuasa *et al* [14] have reported TMR values of $\sim 180\%$ in MgO based Magnetic Tunnel Junctions. The magnitude of the tunnelling MR (TMR) at low temperature is in agreement with the predictions of Julliere's model [1]. This model is based on the difference in the density of states of the two spin directions at E_F of the migratory electrons in the two FM electrodes [15]. A large TMR is predicted when an FM electrode with a high spin polarisation around the Fermi level (E_F) is employed [16].

The motivation for the current research arose from the idea to fabricate an epitaxial thin film stack structure using a combination of Fe_3O_4 and MgO and investigate the role of the MgO barrier layer on the operation of a possible MgO based MTJ. To this end suitable top electrodes had to be chosen to best represent the property of interest. All of the structures were to be epitaxial in nature as it is believed that, experimentally, coherent tunnelling occurs

for a barrier layer grow epitaxially on a FM electrode. Thus, to study the effect of the barrier layer on the spin polarised tunnelling in a MTJ it is advisable to have as favourable an experimental environment as possible.

The first property under investigation was the interface roughness correlation in heteroepitaxial Fe/MgO/Fe₃O₄/MgO/Fe epitaxial thin film stack structure [17]. For this structure the top electrode was chosen to be Fe due to its soft magnetic nature, its coercive field and because it was thought it would act as a good acceptor for the spin polarised electrons from the Fe₃O₄ layer. It was also hoped that in the future an operational MTJ based on these materials would be a reality.

The second property of interest was the effect of the bottom Fe₃O₄ electrode on the magnetoresistance of the top electrode across the nonmagnetic MgO barrier layer of differing thickness [18]. For this investigation the top layer was chosen to be Cr, to form a Fe₃O₄/MgO/Cr structure. It has also been reported that Cr grows epitaxially on MgO [19]. It has been reported that Cr of thickness less than 10 nm is a commensurate antiferromagnetic material [20] and it has a very low positive magnetoresistance (MR). Thus it was expected that the effect of the negative Fe₃O₄ MR on the MR of the Cr top electrode would be readily observable as a function of barrier layer thickness. This should give some indication of the coupling of the two magnetic layers through the nonmagnetic layer thus providing some information about the role of the barrier layer.

Fe₃O₄ was chosen due to its almost 100% spin polarisation, which is a direct consequence of its half metallic nature. Magnetite has attracted much attention as a potential material for FM layers in tunnelling junctions [21 – 25]. The conduction process in Fe₃O₄ will be discussed later and its physical properties will become more apparent. The insulating layer was chosen to be MgO because of the small lattice mismatch, (~0.3%), between Fe₃O₄ and MgO. This small lattice mismatch enhances the probability of epitaxial growth of the MgO layer on the Fe₃O₄ layer. There have been many reported investigations of the epitaxial growth of MgO on Fe₃O₄ [21, 22, 23].

It is also possible to grow epitaxial Fe on MgO, again due to the small lattice mismatch, ~3.5%. The deposition parameters and properties of epitaxial Fe on MgO have also been reported by various investigators [19, 24, 25]. Thus it was envisaged purely epitaxial structures could be constructed. This in itself is quite important because it is believed that, experimentally, coherent tuning would occur for a barrier layer grown epitaxially on a FM electrode [26].

Thus, it was hoped that this research would give some insight into the feasibility of producing a workable Magnetic Tunnel Junction (MTJ) based on a heteroepitaxial $\text{Fe}_3\text{O}_4/\text{MgO}/\text{Fe}$ structure.

Chapter 2: Theoretical Considerations

2.1 Properties of Magnetite

Magnetite is described as an inverse spinel material. It is based on a face centred cubic (fcc) oxygen lattice, with a lattice constant of 8.397 Å. The unit cell is arranged such that the Fe^{3+} cations occupy 1/8 of the available tetrahedral (A) sites and equal amounts of Fe^{2+} and Fe^{3+} ions fill the available octahedral (B) sites. The unit cell consists of 4 (001) layers, each layer contains the oxygen anions and the octahedral Fe ions, the tetrahedral sites are located halfway between these layers. A schematic of the magnetite unit cell is shown in figure 2.1 below [27].

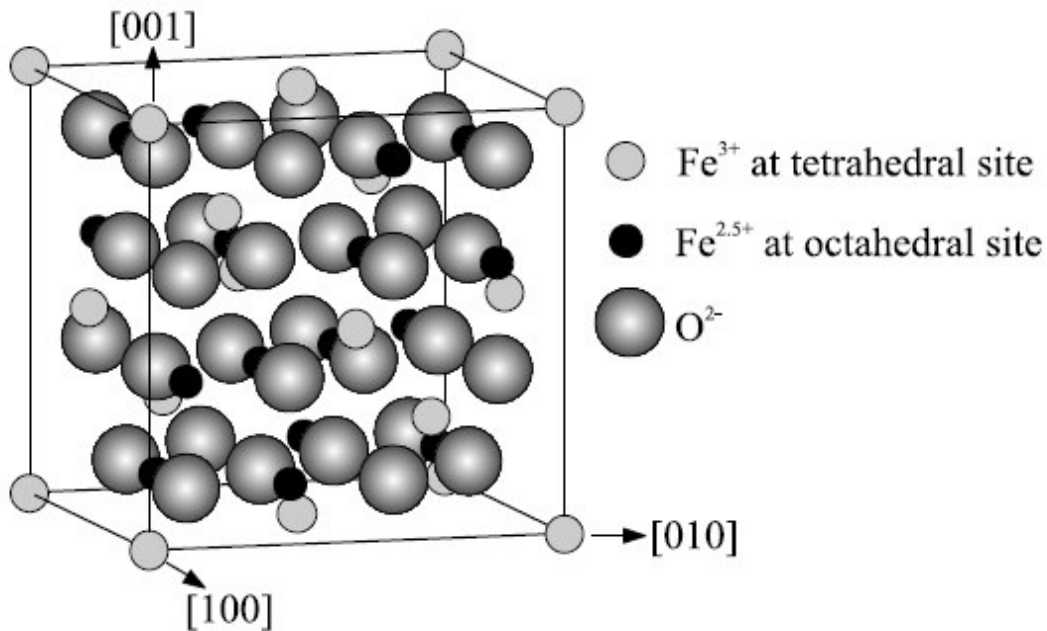


Figure 2.1: Schematic of the Fe_3O_4 unit cell

From figure 2.1 it can be seen that the octahedral (B) sites lie in strings along the $\langle 110 \rangle$ direction. In a (001) plane alternating strings are occupied. Strings in the next layer are rotated by 90° with respect to the one below via a screw axis. Magnetite belongs to the $\text{Fd}3\text{m}$ symmetry group.

The conductivity of magnetite is determined by electron hopping between the Fe^{2+} and Fe^{3+} ions, which occurs at the B sites. This electron hopping results in the high conductivity

associated with magnetite and an average charge of $\text{Fe}^{2.5+}$ associated with the octahedral (B) sites. The tetrahedral sites associated with the Fe^{3+} ions have 5 d-electrons, each with parallel spins due to the filling of the d sub shell in accordance with Hund's Rule. The Fe^{2+} ions, however, have an additional electron and following from convention this extra electron has a spin down orientation. This additional electron can easily hop to a neighbouring Fe^{3+} site if the spins are parallel. Magnetite, when in a magnetically ordered state, only the spin down electrons can easily move. This leads to the idea of a spin polarised electron transport and the notion that magnetite is 100% spin polarised, see figure 2.2 below. From this discussion it should be obvious that electron conduction is restricted to the octahedral (B) sites. The spins associated with the octahedral (B) sites are orientated ferromagnetically because of their mutual antiferromagnetic coupling to the tetrahedral (A) sites.

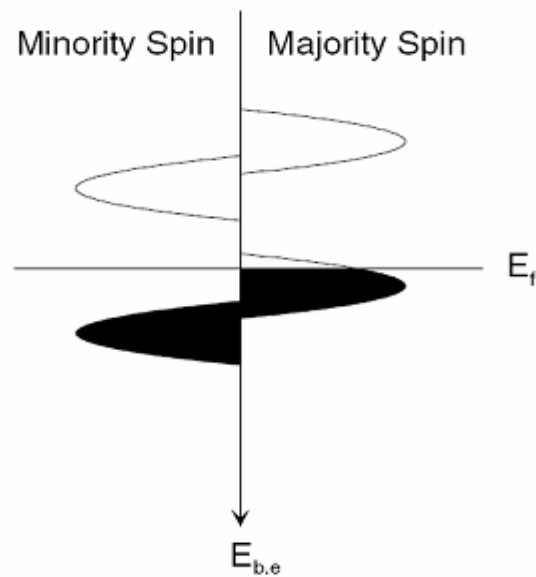


Figure 2.2: Schematic representation of the band structure of magnetite. The 100% spin polarisation of magnetite is due to the population of the majority spin carriers at the Fermi level

Magnetite is also characterised by the presence of a temperature transition, called the Verwey Transition [28]. This transition occurs around 120 K and results in a structural distortion of the magnetite unit cell from its cubic structure. Below the Verwey Transition

temperature charge ordering occurs at the octahedral (B) sites thus reducing the conductivity by two orders of magnitude. The exact transition temperature depends on the film thickness and stoichiometry. The presence of a Verwey Transition in a magnetite film is a good indication of the purity and stoichiometry of the film. Indeed, a simple R-T curve can be used to quickly determine the quality of your magnetite thin film.

2.2 Fe_3O_4 – MgO Lattice Mis-match

For tunnel junctions based on a magnetite electrode MgO is an ideal candidate for the barrier layer. This is due mainly to the small lattice mismatch between magnetite and MgO (mismatch $\sim 0.3\%$), the lattice parameter of MgO being 4.213 \AA . This almost perfect epitaxial relationship between the two is due to their common face centred cubic (fcc) oxygen sub-lattice. MgO possesses the rock salt crystal structure, as shown in figure 2.3, and belongs to the space group $\text{Fm}\bar{3}\text{m}$ [27].

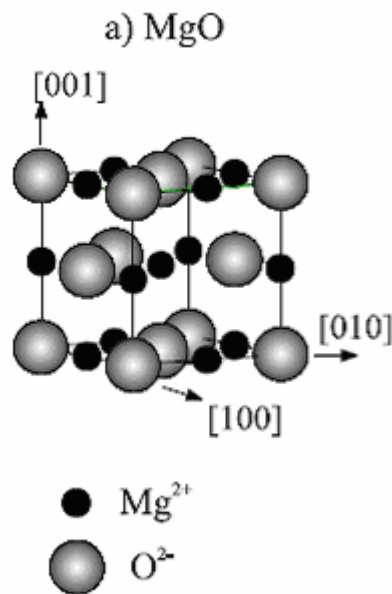


Figure 2.3: Schematic of the MgO lattice, showing its rocksalt structure. The oxygen sub-lattice is the same as that of Fe_3O_4 . All the octahedral sites are occupied by Mg^{2+}

2.3 Properties of the thin epitaxial Cr layer

For the second investigation of the role of the MgO barrier layer in a magnetic tunnel junction an epitaxial thin film of Cr was chosen for the top electrode. It was chosen due to its low, positive MR, as predicted by Abdul-Razzaq *et al* [29]. It was envisaged that the effect of the magnetite electrode on the MR of the Cr electrode, through the MgO barrier layer, would be readily observable.

The magnetic properties of the top Cr layer can be described as being commensurate anti-ferromagnetic. This arises from the fact that Cr thin films exhibit incommensurate spin density wave (I-SDW) properties, with a period of modulation which is much greater than the Cr lattice parameters. Close to the Neel temperature the modulation values reach values of around 100 Å. When the thickness of the Cr layer is reduced to values below the length of one modulation period, at any temperature, a transition from an incommensurate SDW to a commensurate SDW takes place. This has been reported by Zabel *et al* [30] and observed by Fullerton *et al* [31, 32] as well as Schreyer *et al* [33]. Thus, any Cr film of thickness less than 10 nm can be considered to be commensurate anti-ferromagnetic, with magnetisation in-plane. In this investigation we used 5 nm thick Cr films, which easily fall below the thickness limit for the collapse of spin density waves from incommensurate to commensurate.

2.4 Tunnelling Magnetoresistance (TMR)

As previously stated, the first reported MR measurements on a FM – I – FM trilayer junction was made by Julliere [1]. Julliere was also the first to put forward a theoretical explanation for the observed Tunnelling Magnetoresistance (TMR). He interpreted his results based upon a simple model, itself based upon the classical theory of tunnelling where the right (top) and left (bottom) electrodes are independent systems and the barrier is treated as a perturbation, leading to the tunnelling. There were two basic assumptions central to Julliere's explanation.

The first assumption was that the spin of the electrons was conserved in the tunnelling process. From this assumption it is reasonable to assume that the tunnelling of the spin-up and the spin-down electrons are two independent processes, so the conductance occurs in

separate spin channels. According to this assumption, electrons originating from one spin state in the lower ferromagnetic electrode are accepted by unfilled states of the same spin in the upper ferromagnetic electrode. If the two ferromagnetic electrodes have a parallel magnetisation configuration the minority spins tunnel to the minority spin states and the majority spins tunnel to the majority spin states. Conversely, if the magnetisations are aligned anti-parallel to each other the identity of the majority and minority spin states are reversed, so the majority spins of the lower electrode tunnel to the minority spin states in the upper electrode, and vice versa. This process leads to the difference in resistance of the two configurations, as shown schematically in figure 2.4 below.

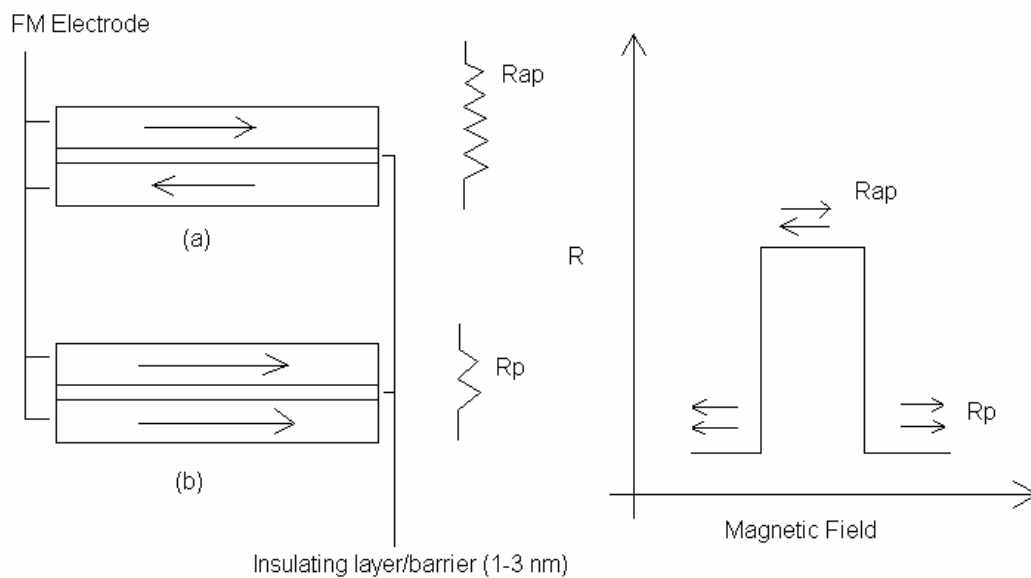


Figure 2.4: Schematic of (a) the anti-parallel magnetisation alignment and (b) the parallel magnetisation alignment in a Magnetic Tunnel Junction and the corresponding resistance as a function of the magnetisation orientation

Julliere's second assumption was that the conductance of a particular spin orientation is proportional to the product of the effective (tunnelling) density of states (DOS) of the two ferromagnetic electrodes. Accordingly, the conductance for the parallel and anti-parallel alignments, G_P and G_{AP} , can be expressed as follows:

$$G_P \propto \rho_1^\uparrow \rho_2^\uparrow + \rho_1^\downarrow \rho_2^\downarrow \quad (2.1)$$

$$G_{AP} \propto \rho_1^\uparrow \rho_2^\downarrow + \rho_1^\downarrow \rho_2^\uparrow \quad (2.2)$$

where ρ_i^\uparrow and ρ_i^\downarrow are the tunnelling DOS of the ferromagnetic electrodes for the majority and minority spin electrons. Following on from these equations it is readily noticeable that the parallel and anti-parallel magnetised MTJs have different conductances, leading to a non-zero TMR. Thus, the TMR is defined as the conductance difference between parallel and anti-parallel magnetisations, normalised by the anti-parallel conductance, i.e.

$$TMR \equiv \frac{G_P - G_{AP}}{G_{AP}} = \frac{R_{AP} - R_P}{R_P} \quad (2.3)$$

from this equation we arrive at Julliere's formula:

$$TMR = \frac{2P_1P_2}{1 - P_1P_2} \quad (2.4)$$

Equation (2.4) predicts that if both FM electrodes have a 100% spin polarisation (i.e. $P_1 = P_2 = 1$) then theoretically the TMR goes to infinity. If one of the electrodes has a 100% spin polarisation then a TMR much in excess of that for a system where none of the electrodes has a 100% spin polarisation is to be expected. This is the rationale for studying a Fe_3O_4 based Magnetic Tunnel Junction (MTJ).

Equation (2.4) can be written to express the TMR in terms of the effective spin polarisations of the two ferromagnetic electrodes:

$$P_i = \frac{\rho_i^\uparrow - \rho_i^\downarrow}{\rho_i^\uparrow + \rho_i^\downarrow} \quad (2.5)$$

However, the Julliere model does not accurately predict the value of the TMR for a particular system due to several reasons. Even so, it is still very valid as it can be used to correlate the magnitude of the TMR with the spin polarisation of ferromagnetic electrodes.

Julliere's model lacks accuracy due to the simple models upon which it was based, namely the classical idea of tunnelling. Slonczewski [34] developed the theory explaining TMR by treating the electrodes and the barrier as a single quantum mechanical system. His method allows one to study tunnelling through low and relatively permeable barriers when the upper and lower electrodes cannot be regarded as totally independent. He developed his approach by realising that in the classical theory the electron wave originating in one of the electrodes becomes evanescent in the barrier but never reaches the other electrode. When the barrier is relatively permeable (low/thin), the evanescent wave functions of the electrons from the upper and lower electrodes overlap in the barrier region and, therefore, need to be matched across the whole junction.

Slonczewski's model is based on tunnelling between two identical ferromagnetic electrodes separated by a rectangular potential barrier. He assumed that the two ferromagnets could be described by two parabolic bands shifted rigidly with respect to one another to model the exchange splitting of the spin bands. Having imposed perfect translational symmetry of the tunnel junction along the layer and matched the wavefunctions of the electrons across the junction, he solved Schrodinger's equation and determined the conductance as a function of the relative magnetisation alignments of the two ferromagnetic electrodes. In the limit of a thick barrier he found that the conductance is a linear function of the cosine of the angle Θ between the magnetic moments of the electrodes, as shown in equation (2.6):

$$G(\Theta) = G_0(1 + P^2 \cos \Theta) \quad (2.6)$$

In the parallel alignment configuration the angle between the magnetic moments of the electrodes reduces to zero, thus reducing the cosine Θ term to 1. This results in a

conductance maximum, which, in a MTJ manifests itself as a resistance minimum. Conversely for an anti-parallel alignment configuration, the angle between the magnetic moments is 180° , reducing the cosine Θ term to -1, thus equation (2.6) reduces to the Julliere formula, equation 2.4 ($P=P_1=P_2$). The term P refers to the effective spin polarisation of the tunnelling electrons and implies the conductance is a function of both the angle between the magnetic moments of the electrons and the spin polarisation of the tunnelling electrons. P , in equation (2.6) above is given by:

$$P = \frac{k^\uparrow - k^\downarrow}{k^\uparrow + k^\downarrow} \cdot \frac{\kappa^2 - k^\uparrow k^\downarrow}{\kappa^2 + k^\uparrow k^\downarrow} \quad (2.7)$$

where k^\uparrow and k^\downarrow denote the Fermi wavevectors of the dispersive bands of the majority and minority spins and κ is the constant of decay of the wavefunction into the barrier, which is determined by the potential barrier height, U , given by:

$$\kappa = \sqrt{((2m/\hbar^2)(U - E_F))} \quad (2.8)$$

The results of Slonczewski's work can be best summarised by saying the spin polarised conduction electrons of one or two-band semi infinite magnetic layers tunnel from one layer to another across a nonmagnetic insulating layer. As a result of this spin polarised tunnelling an effective Heisenberg-like interlayer coupling between the magnetisations of the magnetic layers across a nonmagnetic layer was predicted.

Slonczewski's work has been improved upon by others but such treatments are outside the scope of this work. However, for the purpose of this research the models of Julliere and Slonczewski are perfectly adequate.

2.5 Reflection High Energy Electron Diffraction (RHEED) Theory

While a full kinematic description of the theory of RHEED is beyond the scope of this work the very basics will be presented to allow the readers interpret the RHEED images that will be presented at a later stage. Essentially, diffraction is possible when the following condition is met [35]:

$$k' - k_0 = G \quad (2.9)$$

where k_0 is the incident beam, k' is the diffracted beam and G is the reciprocal lattice vector. This implies that the conditions for diffractions are met when the incident and diffracted wavevectors differ by a reciprocal wavevector. This condition is represented schematically in figure 2.5 below.

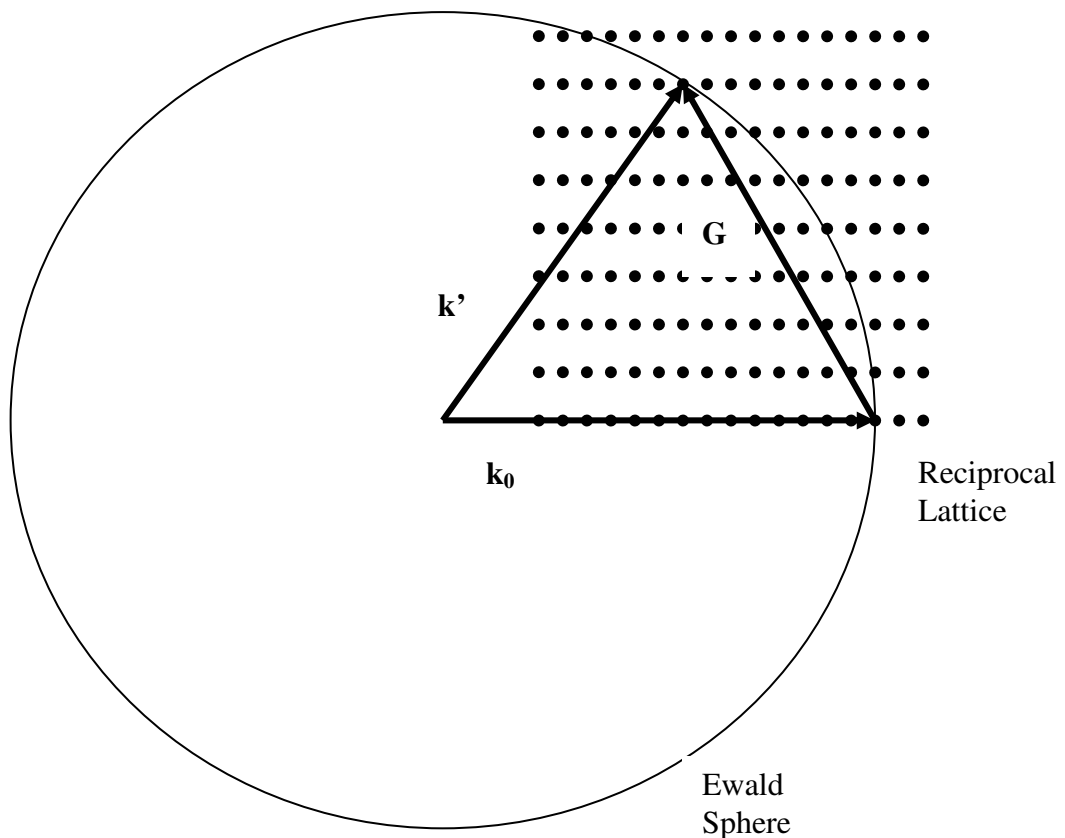


Figure 2.5: Schematic of the requirements necessary for the RHEED diffraction conditions to be fulfilled. The Ewald sphere is a sphere of radius k_0 , centred at the centre of the sample being measured

Due to the glancing angle of the electron beam on the surface of the sample being measured the penetration depth is very small, a matter of a few monolayers. As a consequence of this the lattice can be reduced to a 2D model. The reciprocal lattice for a 2D lattice is a 1D lattice. Thus, for the purposes of RHEED measurements, the reciprocal lattice of the sample being measured can be considered as a series of lattice rods normal to the sample surface. The diffraction pattern observed (on a phosphor screen) is a result of an intersection of the Ewald sphere and these lattice rods. Generally, the Ewald sphere is some 70 times greater than the reciprocal lattice unit. Thus, the intersection of the Ewald sphere with a reciprocal lattice rod is almost tangential. This leads to the elongated streaks associated with a clean, well ordered sample surface. Any degradation of the streaks observed is an indication of a rough, and possibly dirty, surface. In the case where the Ewald sphere is of the same order of magnitude as the reciprocal lattice unit the diffraction pattern is a series of diffraction spots located along a Laue circle. This is represented in figure 2.6 below.

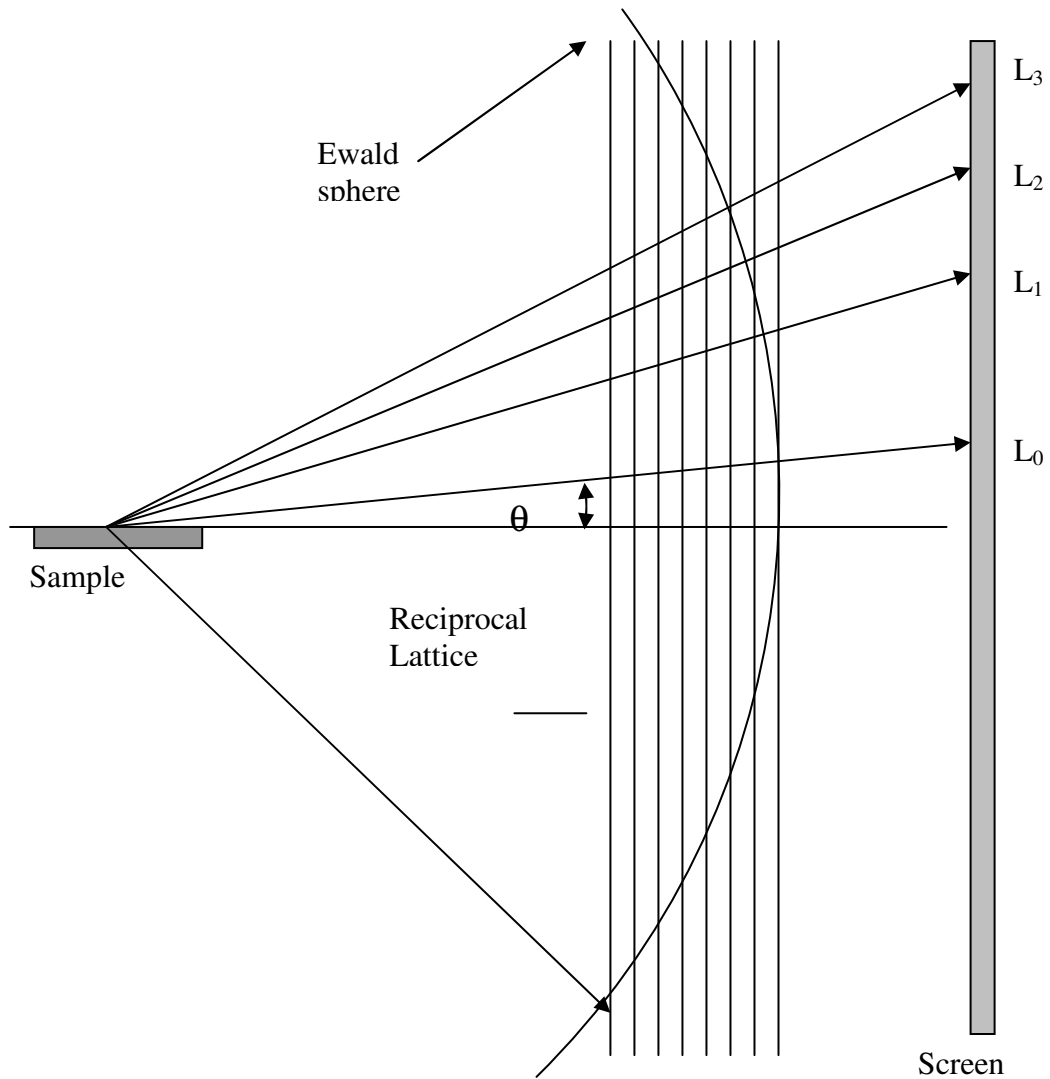


Figure 2.6: Ewald sphere construction and diffraction geometry of RHEED. Intensity maxima on the screen correspond to projected intersections of the Ewald sphere with the reciprocal lattice. The diffraction spots on the screen are located along the Laue circles (intersection of the diffraction cones with the screen)

The RHEED patterns are used to determine the quality of the surface, both the substrate surface and the as deposited films. Since we are dealing with epitaxial films RHEED measurements are ideal for surface quality determinations. The presence of Kikuchi lines in the RHEED pattern are further evidence of a smooth, well ordered surface as the Kikuchi lines are a result of dynamic scattering of the electrons on the crystal surface (theory outside the scope of this study). The Kikuchi lines are degraded by the presence of a rough surface.

2.6 High Resolution X-Ray Diffraction (HRXRD) Lattice Parameter Calculations

The lattice parameter calculations were based on high resolution x-ray diffraction (HRXRD) symmetric and asymmetric diffraction scans. These scans result in the production of Rocking Curves and are based on the $\omega - n\theta$ relationship, where $n = 2$ for symmetric scans and $n \neq 2$ for asymmetric scans. The value of n for the asymmetric scans depends on the geometric configuration used to probe the material and on the strain present in the material. All of the films under discussion in this thesis were epitaxial in nature due to the deposition techniques used, i.e. MBE. This means that the substrate – film system may be represented as shown in figure 2.7.

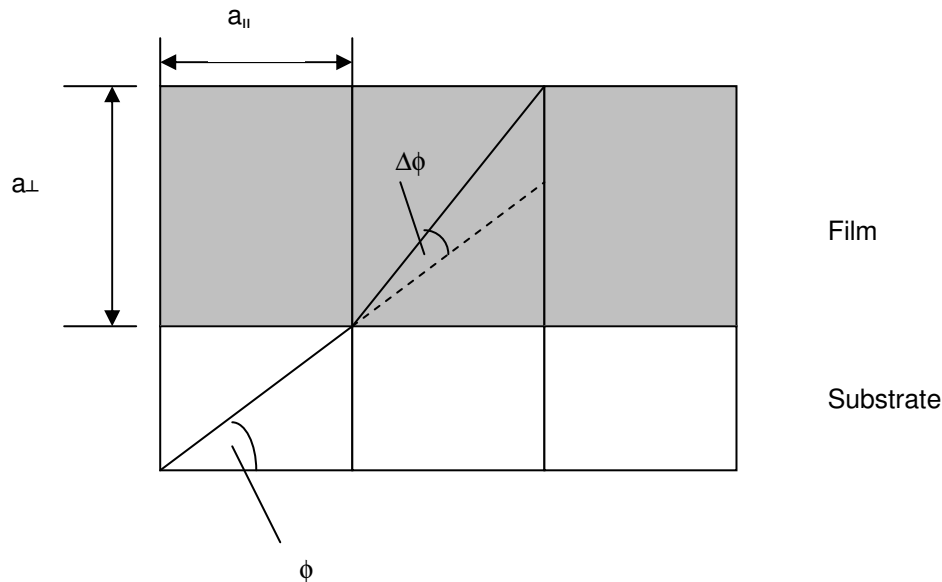


Figure 2.7: Schematic of a fully strained substrate – film system such as $\text{MgO} - \text{Fe}_3\text{O}_4$. The angle ϕ is the angle between the diffracting planes and the film surface.

Thus, two different configurations are required to determine the out-of-plane lattice parameter a_{\perp} and the in-plane lattice parameter a_{\parallel} . The out-of-plane parameter, a_{\perp} , is determined using a symmetric diffraction scan while the in-plane parameter, a_{\parallel} , is determined using an asymmetric scan. The geometries of each scan type are shown in figure 2.8 below, along with the associated scan pattern, i.e. the rocking curve. For the symmetric diffraction scan the Bragg equation for diffraction is used:

$$n\lambda = 2d\sin\theta_B \quad (2.10)$$

In our case the system being investigated using HRXRD is a MgO – Fe₃O₄ system and the symmetric relationship between the diffraction planes is MgO (200) / Fe₃O₄ (400). We are also working in the first order meaning that the n = 1 and equation (2.10) becomes:

$$\lambda = 2d_{Fe_3O_4(400)}\sin\theta_{Fe_3O_4} \quad (2.11)$$

The value for $\theta_{Fe_3O_4}$ is derived from the relationship:

$$\theta_{Fe_3O_4} = \theta_{MgO} + \Delta\omega_{symm} \quad (2.12)$$

Both θ_{MgO} and $\Delta\omega_{symm}$ are measured from the rocking curve and solving equation (2.11), with $\lambda = 1.5406 \text{ \AA}$ (the x-ray wavelength from the Cu K α 1 transition), for the spacing value d we arrive at the following:

$$a_{\perp} = 4d_{Fe_3O_4(400)} \quad (2.13)$$

To calculate the in-plane lattice parameter both the glancing incident and glancing exit diffraction configurations must be taken into account. The value n in the relationship $\omega - n\theta$ is determined by the Bede software which takes into account the strain present in the system as determined from the $\Delta\omega_{symm}$ value. As seen in figure 2.8, from the asymmetric diffraction scans we derive the values $\Delta\omega_{gi}$ and $\Delta\omega_{ge}$, which are used to calculate the in-plane lattice parameter via the following equation:

$$a_{\parallel} = a_{MgO} \left(\frac{\sin\theta}{\sin(\theta+\Delta\theta)} \cdot \frac{\sin\phi}{\sin(\phi+\Delta\phi)} \right) \quad (2.14)$$

where $\Delta\theta$ is the shift from the Bragg angle θ_B due to the strain in the film and $\Delta\phi$ is the change in the angle between the diffraction planes and the surface due to the strain in the system. They are given by the following equations:

$$\begin{aligned}\Delta\theta &= \frac{\Delta\omega_{gi} + \Delta\omega_{ge}}{2} \\ \Delta\phi &= \frac{\Delta\omega_{gi} - \Delta\omega_{ge}}{2}\end{aligned}\tag{2.15}$$

Thus, both the out-of-plane and in-plane lattice parameters were calculated from the high resolution x-ray diffraction data collected.

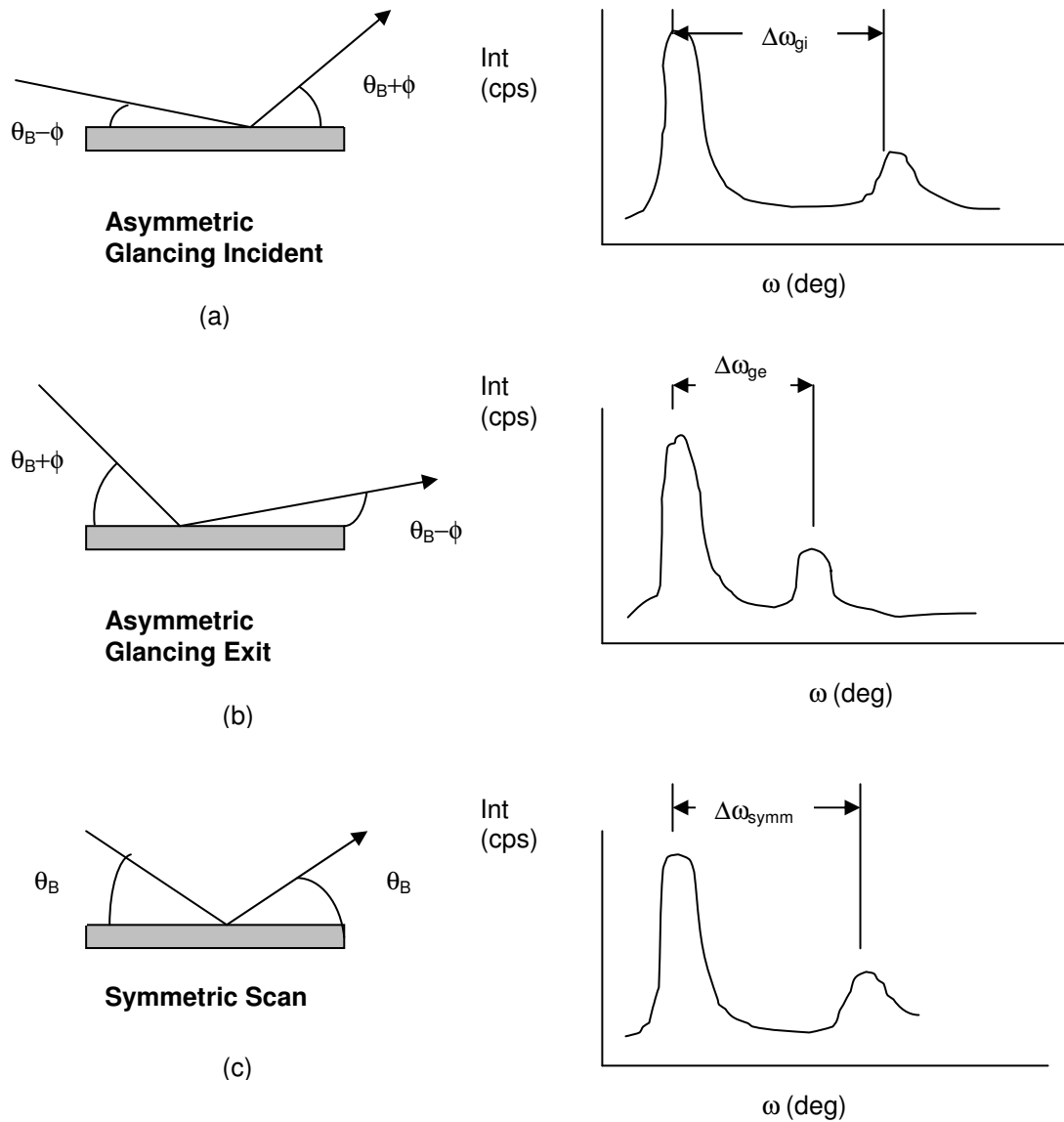


Figure 2.8: The geometrical configurations for the (a) the asymmetric glancing incident configuration, (b) the asymmetric glancing exit configuration and (c) the symmetric diffraction configuration and their associated rocking curves.

Chapter 3: Experimental Details

3.1 Introduction

The study and application of ultrathin films has developed over the last decade due to improvements in ultra high vacuum technology and deposition techniques. One of the most important growth techniques for single crystal thin films is molecular beam epitaxy (MBE). Using MBE thin films can be grown with very precise control over the film thickness and stoichiometry, thus enhancing the reproducibility of quality thin film production. In our MBE system a molecular beam of a metal species is created by the evaporation of the source material using a beam of high energy electrons. The molecular beam subsequently condenses on a substrate and the thin film grows epitaxially. By controlling the flux of the molecular beam, by controlling the energy of the evaporating e-beam, one can control the growth rate of the thin film. Metal oxides may also be grown by MBE by simply adding the appropriate gas into the deposition chamber. The gas may be added in molecular form or, using a plasma generator, may be added in atomic form. In this manner we were able to produce the magnetite films for this research work. The low background pressure possible due to the advances in high vacuum technology ensure that the growing film remains contamination free for the time necessary to deposit the films and analyse them *in situ*.

3.2 Molecular Beam Epitaxy System

All of the films grown and investigated during the course of the research outlined in this thesis were deposited using a DCA MBE M600 Molecular Beam Epitaxy System. The system comprised of two separate chambers connected via a gate valve. The chambers were designated the Load-Lock chamber and the Deposition chamber. Substrates and samples were transferred between the chambers using a magnetically coupled transfer arm, which had a transfer cup attached. The transfer cup facilitated transfer of the bare substrate/sample from the Load-Lock chamber to the Deposition chamber and vice versa. The deposition chamber was fitted with a Reflection High Energy Electron Diffraction (RHEED) system for *in situ* sample analysis. Construction of the system was in all parts UHV compatible while all parts were fitted with standard ConFlat (CF) type flanges for use with flat Copper gaskets. The base pressure of the Load-Lock chamber was of the order 5×10^{-7} Torr while the base

pressure of the Deposition chamber was of the order of 5×10^{-10} Torr. A photograph of the system layout is given in figure 3.1 below.



Figure 3.1: The entire MBE system, including the load-lock chamber, the deposition chamber, the transfer arm and the assorted power electronics cabinets.

3.2.1 Load-Lock Chamber

The Load-Lock chamber design utilises a small volume chamber consisting of a 200 mm ID spherical vessel. The substrate holder is introduced into the Load-Lock chamber via a VITON sealed quick access door (top loader). The Load-Lock chamber is equipped with a 70 l s^{-1} VARIAN turbo pump and a VARIAN Dry Scroll pump. The chamber is vented through a Nupro vent valve and/or the automatic VARIAN vent valve mounted on the turbo pump. The chamber is vented using either nitrogen or argon gas. The vacuum monitoring includes a GRANVILLE – PHILLIPS control unit with a Convectron gauge head and a nude ion gauge head. The maximum baking temperature for the Load-Lock chamber was $150 \text{ }^{\circ}\text{C}$, limited by the VITON sealed quick access door.

3.2.2 Deposition Chamber

The deposition chamber associated with the MBE system was a vertical 600 mm ID chamber with a wire sealed removable top flange. A schematic of the chamber is shown in figure 3.2 below. The substrate manipulator was located vertically in the centre of the chamber meaning that, once loaded the substrate was facing downwards during all processes and manipulations. While the chamber was equipped with two electron guns (e-guns), one magnetron gun and five effusion cells only the two e-guns were utilised. The source materials for evaporation were loaded into individual crucibles, with the composition of the crucible matched to the source material to preclude the risk of damage or contamination. The e-guns were mounted on NW200CF flanges allowing easy access for cleaning. The e-guns were also equipped with external support rails which allowed easy removal of the e-guns and crucibles from the deposition chamber thus facilitating re-filling and servicing. One of the e-guns, designated e-gun #1, was used in conjunction with a single, large crucible which typically contained Fe pellets. The second e-gun, designated e-gun #2, was used in conjunction with a moveable Molybdenum plate which housed four individual small crucible holders. Each crucible was filled with a different source material and the plate, and hence the crucibles, were positioned in relation to the electron beam (e-beam) by means of a feed-through screw. Thus, at any one time the deposition chamber was primed with up to five different source materials.

The electron beam generated by each e-gun was controlled by a sweeper mechanism, which allowed the electron beam characteristics to be adjusted. This allowed the frequency at which the electron beam swept the relevant crucible to be controlled along with the X- and Y-axis travel of the beam over the crucible surface. This was achieved by controlling the voltage applied to plates within the e-gun architecture, thus controlling the deflection of the electron beam. The relevant values were adjusted using a separate, handheld control panel. When the sweeper functionality was in an off position the electron beam fell on only one point of the crucible.

The e-gun power and hence the deposition rates were monitored and controlled using an INFICON IC/5 deposition rate controller. In general, the higher the power applied to the e-gun the more intense the electron beam and thus the higher the deposition rate. Alternatively, the deposition rate could be controlled using the sweeper module. The energy density of the electron beam could be controlled by adjusting the area of the crucible upon which the electron beam fell. The smaller the X- and Y- travel of the beam the higher the electron beam density and so, the same deposition rate could be achieved for a lower power rating. In general this method was not used as the electron beam was set to sweep the entire crucible surface to try and maintain uniform heating of the source material and minimise the effects of local hot spots.

Each e-gun had a port associated with it to house a quartz crystal monitor head. These crystal monitor heads were positioned such that they were shielded from other sources. Each crystal monitor head was further shielded by a shutter which, when used correctly, acted to prolong the lifetime of the monitor head. Each e-gun also had an associated shutter positioned over the relevant crucible evaporation position. This shutter acted to allow material impact on the crystal monitor head but not on the substrate. This in effect allowed the system to be stabilised before deposition commenced. Also associated with each e-gun was an unique beam spot observation system based on a rotatable mirror configuration, Thus, the respective mirrors could be hidden during deposition, to avoid damage or contamination, by means of a rotary feed-through.

The shutter system as described above was a linear electro-pneumatic shutter system. The shutter blades were moved outside the vacuum with a pneumatic actuator. The construction was designed to give enough driving force even after heavy contamination of the shutter blade. The shutter operation was completely controlled using Festo controllers which allow for easy adjustment of the shutter motion via adjustable pressure valves. The shutters were run in soft-mode to minimise vibrations and flake fallings. The deposition chamber also consisted of a main shutter positioned directly below the substrate manipulator. This shutter allowed all beams to be interrupted at once, no matter the source. This shutter was only

opened during the loading of a substrate and during deposition. At all other times it was kept closed to prevent any unwanted material or contaminate impinging on the substrate.

The electron gun area was separated from the main body of the deposition chamber by a water cooled roof. The lower part of the deposition chamber was fitted with a water cooled shroud that effectively separated the growth area from the e-guns. At the lower end of the water panel the source positions were separated from each other with double wall Mo beam separator plates. These plates were in good thermal contact with the water panel and the double walled design effectively prevented any thermal or chemical cross talk between different sources.

The deposition chambers pumping system consisted of a VARIAN Triode ion pump with a pumping speed of 500 ls^{-1} , a VARIAN V1000 1000 ls^{-1} turbo pump and a VARIAN Tri Scroll 600 dry scroll vacuum pump. The turbo pump was separated from the deposition chamber with an electro-pneumatic gate valve via a NW200CF flange. The vacuum system thus described allowed pressures of the order of 5×10^{-10} Torr to be achieved in the deposition chamber.

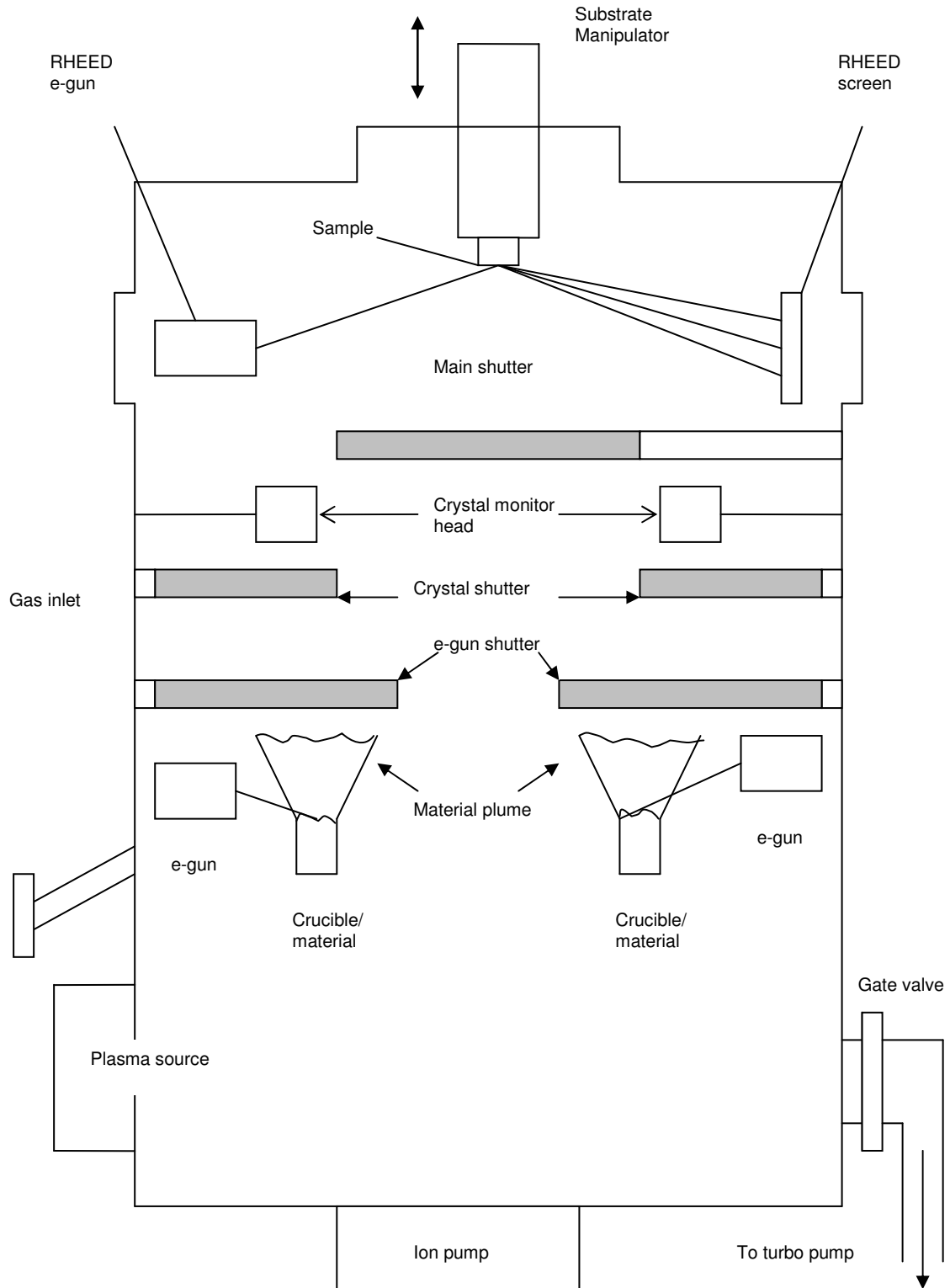


Figure 3.2: A rough schematic of the MBE deposition chamber layout, depicting the RHEED system, the e-guns and the associated shutters and crystal monitor heads, and the vacuum system.

3.2.3 Substrate Manipulator

The system was fitted with a low wobble substrate manipulator which consisted of a heavy duty Z-manipulator, a hollow shaft inverted rotary motion feed-through and a high temperature heater stage. The rotary drive consisted of two concentric tubes of which the inner was stationary and the outer could be rotated, using magnetic coupling. All electrical wiring (thermocouple and power) were conducted through the inner stationary tube.

The substrate manipulator featured a new design for the heater electrical contacts and the support bearings. The heater stage was a high temperature heater stage with a PBN/PG/PBN cup heater element. The element was surrounded by a radiation shield. A C-type thermocouple (W/Rh) was located in the space between the filament and the substrate. The temperature was controlled via a EUROTHERM 2408 controller used in conjunction with a DC power supply. All pre-deposition annealing was done *in situ* using the substrate manipulator heater negating the need for a separate annealing chamber. This improved the quality of the cleaned substrates and minimised possible contaminants that may have arisen as a result of the transfer procedure between adjacent chambers.

The heavy duty Z-stage was used for loading and RHEED alignment purposes. The manipulator also allowed the substrate to be lowered to any height above the main shutter thus increasing the effectiveness of the main shutter in interrupting all e-beams. The attachment of the substrates to the sample manipulator and the RHEED system alignment will be discussed in later sections, suffice to say that the substrates were loaded into Molybdenum holders which in turn were loaded into the substrate manipulator with a minimum of stress and the active substrate surfaces were pointing down and held in place by gravity alone. The Molybdenum holder allowed for low electron beam incident angle RHEED measurements to be made and the special features associated with the substrate manipulator that facilitated these measurements are as follows:

- open axis rotary drive
- secondary tilt not needed for substrate loading or flux calibration

- rotary drive had wide bore coated bearings especially designed for high temperature and UHV use
- the first set of bearings far away from the heater stage, thus prolonging the system lifetime
- use of a DC power supply prevents interference with RHEED measurements
- minimised out gassing due to the use of coated UHV bearings and MBE compatible materials
- magnetically coupled rotary drive

The substrate manipulator specifications are:

- continuous rotation
- 50 mm linear Z movement
- maximum 1 inch sample size
- PBN/PG/PBN cup heater element
- Maximum actual substrate temperature 100 C with main shutter closed
- Temperature homogeneity better than ± 5 K at 700 C
- Temperature stability better than ± 2 K over 8 hours at 600 C
- Temperature control with a thermocouple located between the substrate and the filament
- EUROTHERM 2408 programmable temperature control unit and 1 kW DC power supply (temperature read-out with 0.1 K accuracy)

3.2.4 Water Cooling System

All of the water-cooled equipment associated with the MBE system had its own separate water-cooling circuits. The main water-cooled pieces of equipment were the e-guns and the substrate manipulator. The cooling lines were controlled by manual ball valves located in a cooling block. Namur type sensors monitor the water lines to ensure there was sufficient water to cool the respective equipment. There was a safety interlock system to ensure sufficient water cooling. A compressed air line was used to ensure sufficient air pressure to provide sufficient water pressure. Failures of the water pressure lead to tripping of the

interlock and system shutdown. The interlock feature will be discussed below. To try and ensure against water pressure failure the mains water was double filtered before entering the system. The filters were changed on a regular basis, depending on system use and filter degradation.

3.2.5 Interlock System

The system was fitted with an interlock system to safely shutdown the system in the event of a disruption to the cooling water supply or turbo pump failure. In the case of the minimum water flow not being achieved the interlock system instructed the e-gun controllers to shut down the high voltage and filament supply. It also instructed the EURO THERM 2408 controller to shut down the substrate heater power supply. Thus, all the high voltage elements of the system were safely shut down in the event of a water pressure failure. In the event of a deposition chamber turbo pump failure the interlock system instructed the system to close the deposition chamber – turbo pump gate valve, thus maintaining the integrity of the deposition chamber. Such a failure was detected by the gate valve controller when a pre-defined speed threshold value for the V1000 pump was breached. After a power shutdown had occurred the interlock system and possibly the coolant system had to be re-started. It was possible to override the interlock system but this was never done during the course of the research under discussion. The e-guns were also fitted with a separate interlock system to ensure that all relevant electrical safety precautions were adhered to before, during and after operation of the e-guns. The following three conditions had to be fulfilled before the e-guns could be operated:

- the transformer box of the high voltage supply had to be closed
- the high voltage plug cover at the e-gun had to be in place
- the sweeper unit had to be ready for operation

Failure to comply with any of these conditions resulted in an inability to operate the g-guns.

3.2.6 Reflection High Energy Electron Diffraction (RHEED)

The deposition chamber was fitted with a Staib Instrumente Reflection High Energy Electron Diffraction (RHEED) RH 30 system for *in situ* analysis of the substrate and samples under investigation. The system consisted of an electron gun (e-gun) fitted to one of the spare radial deposition chamber ports via a standard UHV 35 CF flange (2.57" OD) and a phosphor screen located diagonally across from the e-gun, fitted to one of the other spare deposition chamber ports. A digital camera was mounted behind the screen to capture the RHEED images. The electron beam source and detector, effectively the e-gun and the phosphor screen, were located along the same axis as was required for the proper operation of the RHEED system. A general schematic of the RHEED configuration is given in figure 3.3, below. The RHEED system was capable of working in UHV and also in a vacuum of the order of 5×10^{-5} Torr, though at this pressure the RHEED electron gun (e-gun) was pumped under a differential arrangement by the load-lock turbo pump. This was done in order to prevent oxidation of the RHEED e-gun element. Specifics of the RHEED system included:

- a small focus spot ($< 100 \mu\text{m}$)
- the beam size remains constant even over large working areas
- a small beam divergence (under 0.2 mrad) could be obtained

All of the components of the RHEED system were UHV compatible, with all the electron optical components baked out in a vacuum oven prior to assembly. The RHEED system was equipped with an electron optical system specially designed for RHEED applications, i.e. it was equipped with an electron optical diaphragm system thus producing as shallow angle electron beam as possible. The electron beam position and size could be controlled by adjusting any of the major electronic parameters, which are:

- **filament** - the filament temperature governed by the power supply current applied, which in turn governed the beam brightness
- **grid** - governed the beam "current" and beam diameter
- **focus** – governed the position of the focus and the beam divergence

All of these parameters were controlled using a separate, handheld control panel. Thus, by optimising the beam brightness, shape and position by correctly choosing the relevant parameters clear, sharp RHEED images could be obtained of the sample surface. For all the RHEED images presented in this work the RHEED system was operated at a voltage of 20 kV and a **filament** current of 1.6 Amps. All other parameters were adjusted on an individual basis in order to produce the best images. It must be noted that due to the proximity of e-gun #1 to the RHEED e-gun high quality RHEED images could not be produced while e-gun #1 was operating. This was due to the effect of the e-gun sweeper fields on the RHEED electron beam. Thus, RHEED images for films grown using e-gun #1 were only taken on completion of the deposition, with the sweeper in the off position. No such problems arose with the concurrent operation of the RHEED system and e-gun #2.

To complete a RHEED analysis the substrate had to be rotated to ensure the correct crystal orientation was presented to the electron beam. This was achieved by rotating the substrate manipulator through pre-defined angles in order to present the $\langle 110 \rangle$ and the $\langle 100 \rangle$ directions to the e-beam. To ensure reproducibility the substrate manipulator was rotated through a multiple of angles to ensure several manifestations of the same crystal directions were investigated.

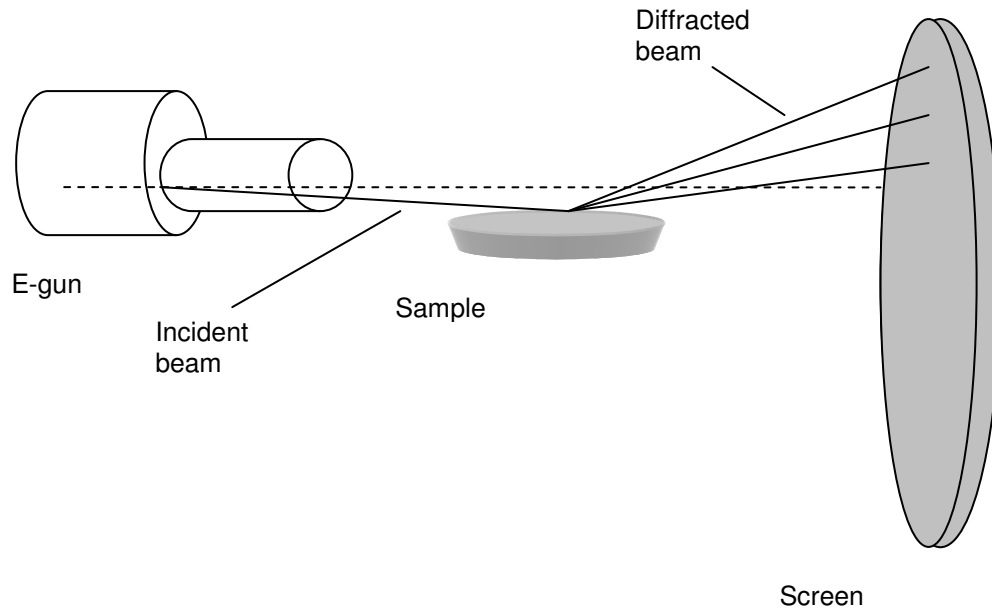


Figure 3.3: Schematic of the RHEED system configuration. The e-gun and the screen lie along the same radial axis of the deposition chamber thus the diffraction conditions are met and a diffraction image appears on the phosphor screen.

3.2.7 Plasma Source

The MBE system was fitted with an Oxford Scientific OSPrey Plasma Source set to operate in Atomic Mode. The plasma source was fitted to the deposition chamber via a CF100 port. Microwaves with a frequency of 2.45 GHz were generated by a microwave magnetron operating at a magnetron power of 30 mA. The microwaves were then coupled through a resonant coupler into a coaxial feed-through structure which guided the microwaves into the vacuum and up into the plasma chamber. The plasma was excited in this chamber and the microwaves absorbed. The plasma was confined to this chamber. Further enhancement of the plasma density was provided by a magnetic quadrupole arranged around the discharge chamber. This generates an 87 mT surface inside the plasma at which field strength electrons in a 2.45 GHz microwave field undergo electron cyclotron resonance motion. The spiralling motion greatly enhanced the electron path length and therefore the probability of collisions leading to the creation of ions was increased. The open end of the plasma chamber was fitted with aperture plates with a number of small holes. These acted to reduce the

number of ions leaving the plasma chamber thus effectively reducing the ion current. The beam leaving the plasma chamber consisted mainly of molecular and atomic particles. In this manner molecular oxygen (O_2) was converted into atomic oxygen and subsequently introduced into the deposition chamber. The atomic oxygen impinged on the surface of the substrate in the same manner as the metallic species and in such a manner thin film metallic oxides were deposited. For this work the only metallic oxide deposited was magnetite.

3.3 High Resolution X-Ray Diffractometer

The high resolution x-ray diffractometer used to perform all of the high resolution x-ray diffraction (HRXRD) measurements was a Bede D1 diffractometer. A schematic of the system layout is given in figure 3.4 below, while a photograph of the actual system is given in figure 3.5. The entire system was housed in a safety case with access to the relevant elements via an assisted opening lid coupled to an interlock system. Essentially the system comprised three main elements, the source stage, the sample stage and the detector stage.

The source or beam stage, which was fixed to the system housing and comprised of all the beam conditioning mechanisms and the related optics required to ensure a homogeneous x-ray beam of small angular dispersion. With correct optimisation of the source stage optics a sub millimetre beam could be achieved that maintained its integrity over long distances (~150 cm). The x-rays were produced from a Cu $K\alpha_1$ transition and had a wavelength of 1.5406 Å. The intensity of the x-ray beam could be controlled via a system of removable metal slits that could be placed in front of the source stage. The relevance of this shall become apparent shortly. There was also a shutter associated with the source stage. If at any time during the operation of the system an attempt was made to open the safety lid without first closing the x-ray shutter, thus isolating the x-rays from the system, the interlock shut the entire system down. This was to ensure that there was no inadvertent x-ray leakage from the system.

The sample stage was a two part system with the main part mounted on a moveable table that allowed it to move in three separate directions, as indicated in figure 3.4. The sample stage was completed by a removable metal disk whose centre was marked via cross hairs

etched into its surface. The sample for analysis was mounted onto the metal disk using double sided tape. The metal disk was magnetically coupled to the main sample stage. The three angles of movement were denoted ω , ϕ and χ . The ω angle was the angle through which the sample stage could move around the z-axis and it had a range of $\sim 90^\circ$ with a resolution of 0.18 arcsecond. The ϕ angle was denoted the rotation of the sample and referred to rotation of the sample around the y-axis. It had a range of 280° and a resolution of 0.18 arcsecond. The χ angle was denoted the tilt of the sample and referred to rotation of the sample around the x-axis. It had a range of 40° and a resolution of 0.01° . Adjustment of these three parameters constituted alignment of the diffraction planes in relation to the source x-ray beam.

The detector stage was also mounted on a moveable platform and was also capable of rotation through a range of angles denoted 2θ . The detector axis rotation range was 235° with a resolution of 0.18 arcsecond. The Bede D1 system was fitted with an EDRc detector with a dynamic range of 0.5 cps to 50 Mcps, though the best results were obtained when the beam intensity was conditioned to give 250,000 cps. The beam intensity could be controlled using the metal slits mentioned above. The system was remotely controlled with all parameters chosen using the Bede Control software provided with the system. All the analysis software was also provided with the system. A further stage was also provided and it acted to further condition the beam thus increasing the system resolution. This stage was the channel cut crystal stage and was positioned in front of the detector. It was only possible to use the channel cut crystal stage when the signal strength was sufficiently strong.

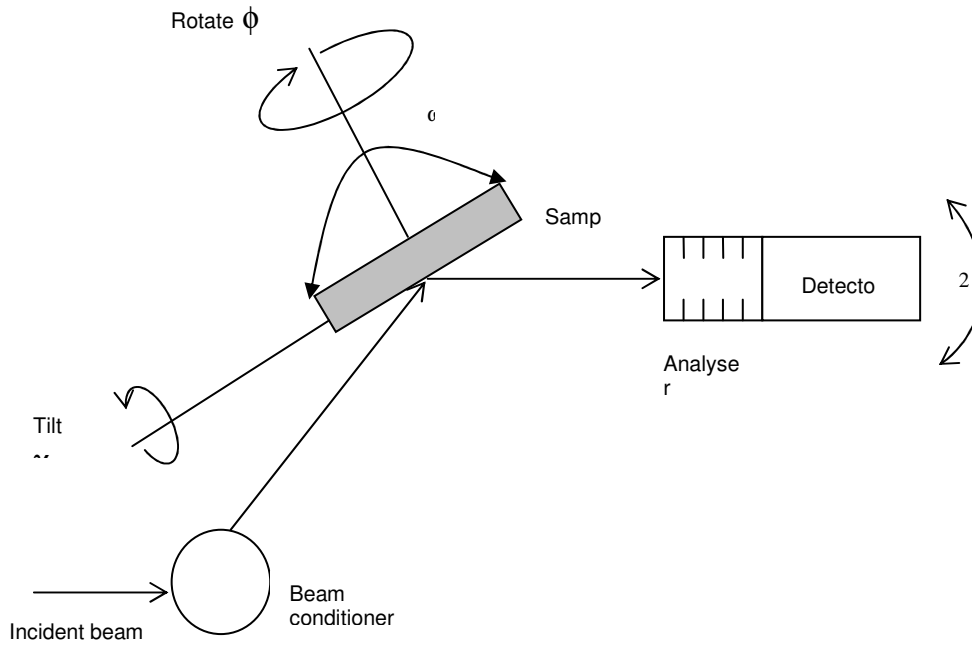


Figure 3.4: A schematic of the Bede D1 diffractometer layout. All of the angles of rotation as described in the main text are outlined. The analyser is a series of removable metal slits used to control the intensity and angular dispersion of the x-ray beam.

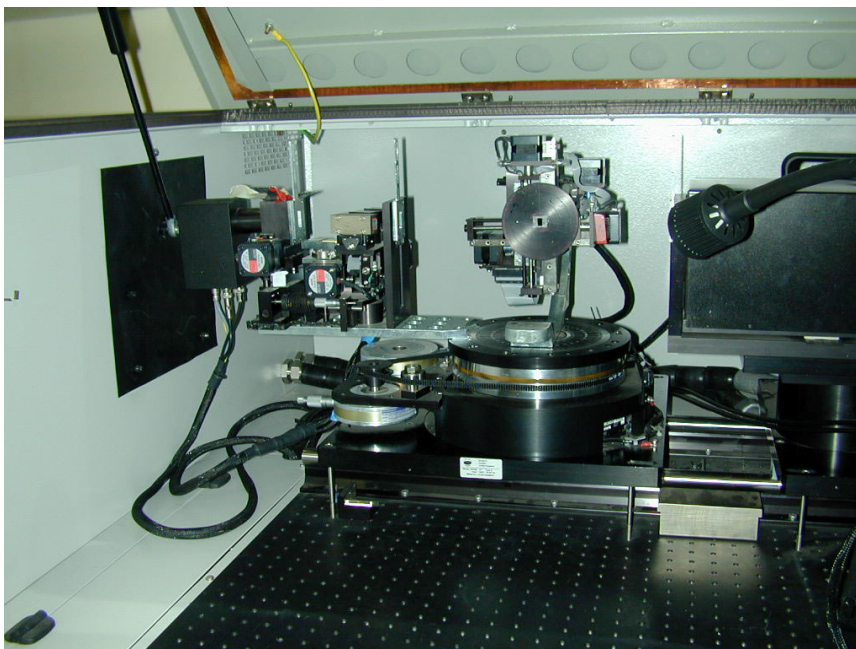


Figure 3.5: Photograph of the components of the High Resolution X-Ray Diffractometer. The sample stage, including the metal sample holder, and the detector stage are visible. The safety lid (open) is also visible.

The two measurements made using the HRXRD were diffraction scans (also known as Rocking Curves) and reflectivity scans. As has been mentioned in the theory section the diffraction scans were used to determine the lattice parameters of the film under discussion. For the course of this work all the HRXRD diffraction scan measurements were made on MgO / Fe₃O₄ based system. The relationship between the diffracting planes of the two materials was MgO (200) / Fe₃O₄ (400) for symmetric scans and MgO (113) / Fe₃O₄ (226) for asymmetric scans. The measurements performed, along with a brief description, are given in Table 3.1 below.

Measurement Name	Explanation
Double Axis Diffraction Scan (Symmetric Scan)	Typical ω - 2θ scan where the ω and 2θ values are obtained from the literature and depend on the plane being measured. Used to calculate the out of plane lattice parameter. The CCC stage was not used.
Triple Axis Diffraction Scan (Symmetric Scan)	Same as the double axis scan but with the CCC stage in position. Provided increased beam resolution allowing for a more accurate peak location.
Glancing Incident Diffraction Scan (Asymmetric Scan)	Measurement of the in plane lattice parameter where the x-ray beam incident angle on the sample was small.
Glancing Exit Diffraction Scan (Asymmetric Scan)	Measurement of the in plane lattice parameter where the x-ray beam incident angle on the sample was large.
Reflectivity Scan	Measurement in which the surface of the sample is probed and from the position of interference fringes the thickness of the sample film was calculated.
Reciprocal Space Map	A series of ω - 2θ scans, where for each scan the ω value is changed slightly. Used to infer information about the strain of a film.
Reflectivity Reciprocal Space Map	A series of reflectivity scans used to build up a picture of the roughness of a sample surface and the roughness correlation between interfaces in a multilayer structure.

Table 3.1: Description of the XRD measurements performed during the course of this research

3.4 Closed Cycle Refrigeration (CCR) system

All of the transport and magnetotransport measurements were performed using a home-made Closed Cycle Refrigeration (CCR) system, a schematic of which is shown in Figure 3.6, below. Figures 3.7 and 3.8 show photographs of the CCR system, with figure 3.7 showing the measurement head while figure 3.8 is a more complete photograph, incorporating the

temperature range of 30 K to 300 K was possible. The entire system was computer controlled and both the R-T and MR measurements were automated.

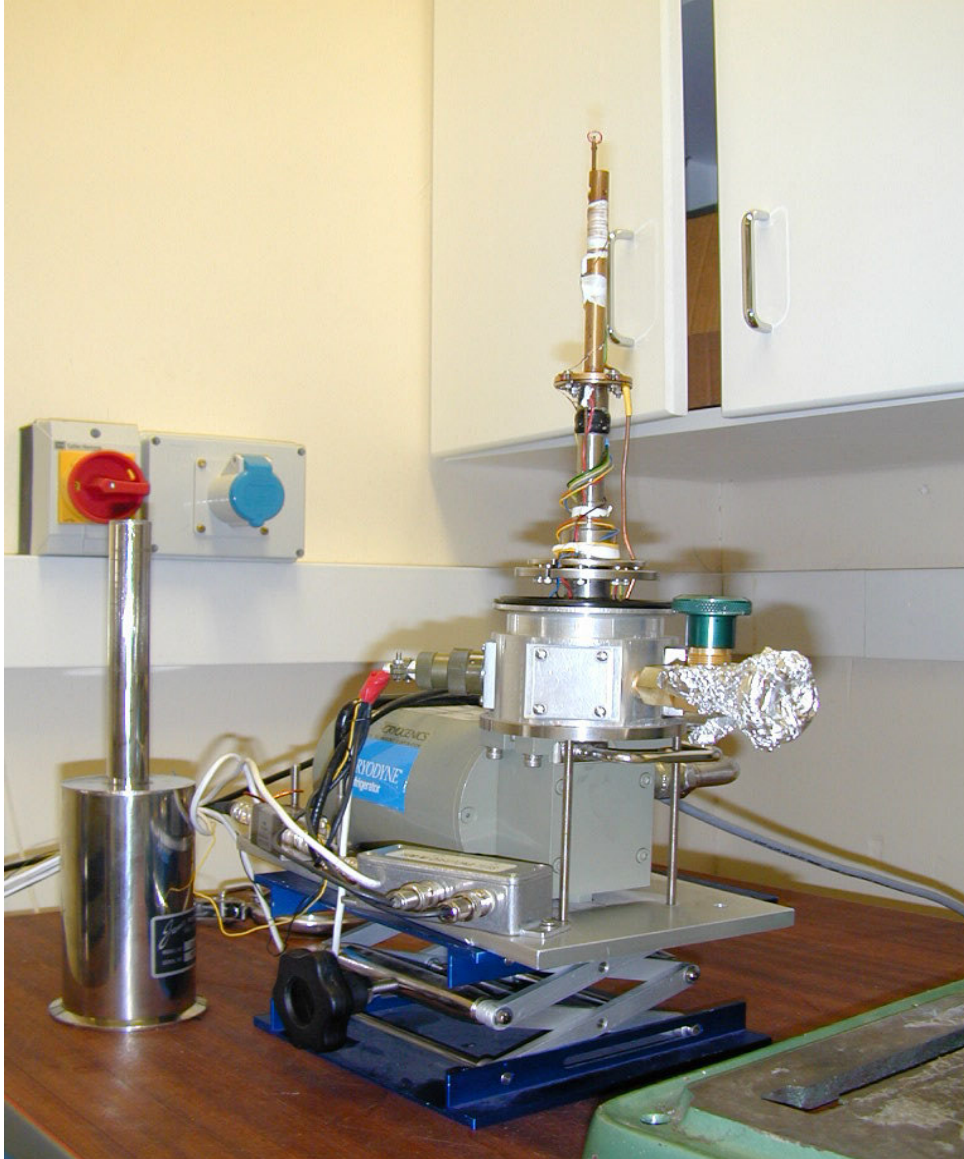


Figure 3.7: Photograph of the CCR measurement system, with the CCR measurement head visible.



Figure 3.8: Photograph of the CCR system in MR measurement configuration. The measurement head is inserted into the permanent magnet.

3.5 Sample Preparation and Loading

Each substrate (MgO substrate) was de-greased in an ultra sonic bath for 20 minutes in each of Acetone, Methanol, Ethanol and Iso-Propanol. The substrate was then boiled in Acetone for several minutes prior to being loaded into the Molybdenum (Mo) substrate holder, shown in figure 3.9 below. The substrate was loaded with the polished side facing down. The Mo holder, and substrate, was then transferred to the transfer cup in the Load-Lock chamber via the VITON sealed quick access door (top loader), using a specially designed transfer tool that

accompanied the MBE system. Once loaded the Load-Lock chamber was pumped until the pressure reached $\sim 5 \times 10^{-7}$ Torr, at which point the gate valve was opened and the transfer arm was moved to a position in the centre of the Deposition chamber. The substrate manipulator was lowered over the transfer cup until it coupled with the Mo substrate holder. The manipulator was then turned through a pre-set angle into the lock position at which point the substrate holder was deemed to be locked into the substrate manipulator substrate holder. The substrate manipulator was then raised again and the transfer arm, and transfer cup, withdrawn from the Deposition chamber. Once the transfer arm was completely removed from the Deposition chamber the gate valve was closed and the two chambers were essentially independent from each other again.

Once the substrate was loaded in the substrate manipulator substrate holder the Deposition chamber was pumped until it again reached its base pressure of $\sim 5 \times 10^{-10}$ Torr. Only at this point did the *in-situ* annealing commence. Generally the substrates were annealed at 600 C in UHV for 30 minutes and in an oxygen environment of 1×10^{-5} Torr at 600 C for 180 minutes. The substrates were annealed in an oxygen environment to ensure that any oxygen vacancies that may have arisen due to the UHV annealing were corrected for. On completion of the annealing the substrate surface was checked using RHEED to ensure the surface was smooth, clean and well ordered. In the event of any problem with the surface the substrate was annealed for a longer duration until a satisfactory RHEED image was obtained. The substrate was then deemed ready for deposition. The deposition parameters used for each structure shall be discussed in the chapter dedicated to the relevant structure.

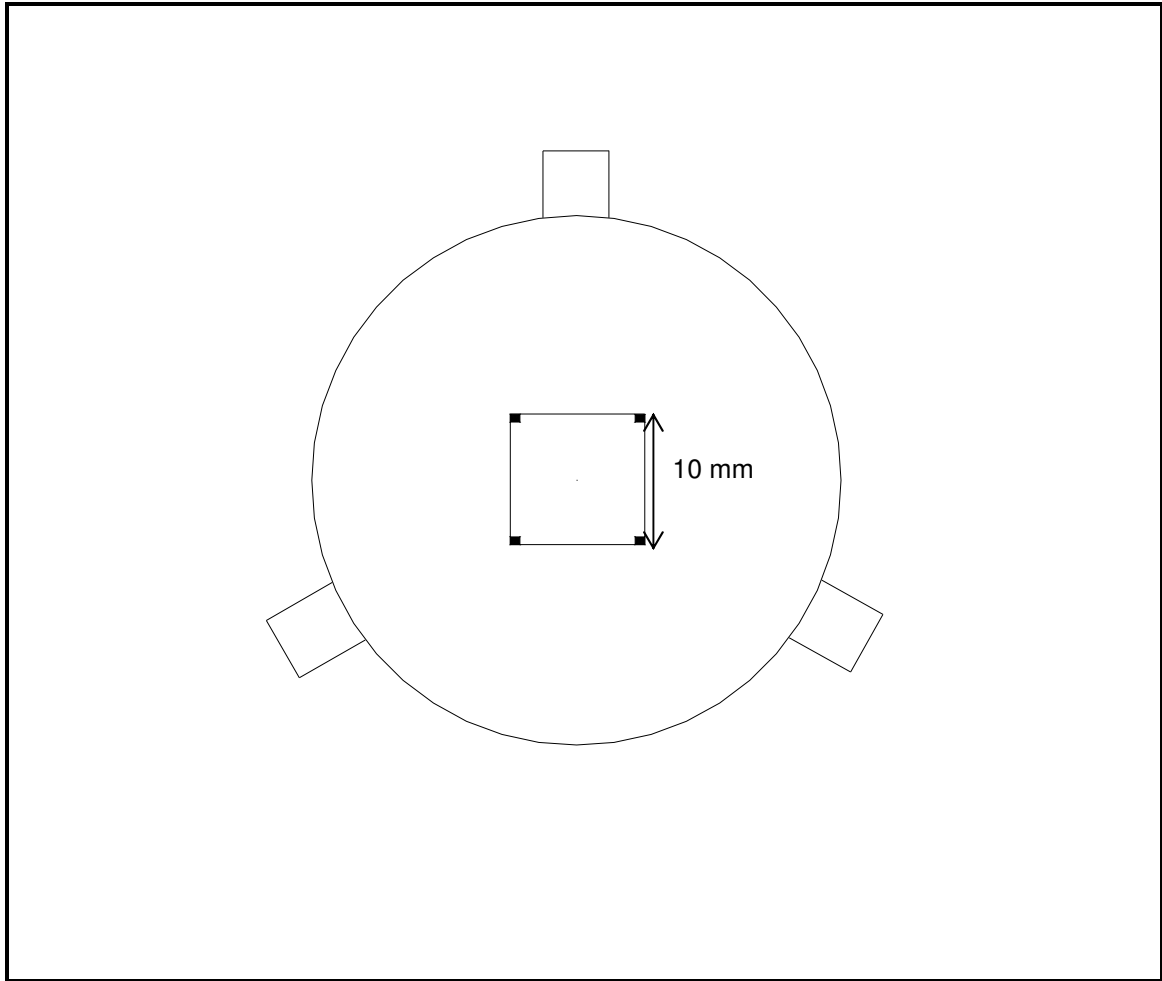


Figure 3.9: Schematic of the Mo substrate holder. The substrate is supported at its edges by the supports shown in the diagram. The centre square is 10 mm x 10 mm.

Chapter 4: Fe₃O₄/MgO/Fe Epitaxial Thin film Stack

4.1 Introduction

The growth and interface roughness correlation in heteroepitaxial (15 nm) Fe₃O₄ / (0.95 – 2.0 nm) MgO/ (10 nm) Fe / (25 nm) Au structures were investigated. The evidence of the correlation of layer interface roughness was found for the thickness of the MgO insulating barrier layer thinner than 0.95 nm but not for the MgO layer thicker than 2 nm. The change in the interface roughness correlation for the thin film stack structure is thought to result from a change in the growth mode of the MgO layer. The results suggest that the correlation of interface roughness may play a role in the thickness dependence of the MgO insulating barrier layer on the electrical properties of tunnelling junctions.

The structure, magnetic and electrical properties of MgO based junctions have been reported [14, 36, 37 and 38]. Magnetic tunnel junctions based on epitaxial films are of great interest as they represent model systems for both experimental and theoretical studies. These are of great interest in so much as they may provide an insight into the fundamentals of the mechanisms associated with spin dependent transport. The interface roughness and roughness correlation between interfaces in a stack structure are thought to be critical for their spin dependent transport properties. This is primarily thought to be because central to the operation of a MTJ is the notion of coherent spin-polarised tunnelling, where the symmetry of the electron wavefunctions plays an important role. It is thought that in well ordered and smooth interfaces the coherency of the wavefunctions is conserved cross the tunnel barrier.

It is known that the ability to directly measure the topological relationship between buried layers is critical for improving the performance of magnetic tunnel junctions [39, 40, 41 and 42]. This work deals with MgO (100)/Fe₃O₄/ MgO /Fe stack structures. The aim was to investigate the extent of the correlation between topologies of the interfaces of the structure and its dependence on the thickness of the MgO barrier layer and the growth conditions. Correlation between the roughnesses of the interfaces gives a good indication of the uniformity of the MgO barrier layer on the micro- and nanometer scale. The uniformity of the

barrier layer in a magnetic tunnel junction is another factor thought to be of critical importance to the efficient operation of MTJs. Indeed, in the commercial world it is thought that MgO barrier layer tolerance thickness uniformity is of the order of 0.2 nm [43].

4.2 Structure Growth and Characterisation

(15 nm) Fe₃O₄/ (0.95 – 2.0 nm) MgO/ (10 nm) Fe / (25 nm) Au structures were grown on MgO (100) single crystal substrates by Oxygen-Plasma-Assisted Molecular Beam Epitaxy (MBE). The deposition system and substrate annealing procedure are given in the Experimental Details chapter. The Au layer in the junction structure acts as a protective layer to prevent the oxidation of the top Fe electrode. The miscut angle of the MgO substrate was less than 0.2°. The base pressure of the MBE system was lower than 5×10^{-10} Torr, putting it in the UHV category.

Briefly, the growth conditions for the various layers and electrodes under discussion were as follows: The Fe₃O₄ layer was deposited by means of e-gun evaporation from Fe pellets with a purity of 99.995% in a plasma oxygen environment of 1×10^{-5} Torr at a substrate temperature of 250 °C. The MgO layer was deposited from MgO pellets of 99.9% purity under similar conditions at a substrate temperature of 400 °C. The Fe film was deposited in a vacuum of 5×10^{-8} Torr at a substrate temperature of 250 °C. The deposition rates were 0.3, 0.02 and 0.1 Å/s for the Fe₃O₄, MgO and Fe layers respectively. The growth rate was controlled using an INFICON IC-5 process controller and quartz thickness monitors. The growth of the junction structures was monitored using *in-situ* Reflection High Energy Electron Diffraction (RHEED). The structure of the thin films was characterized by means of High Resolution X-Ray Diffraction (HRXRD) (Bede D1 System). The interface roughness and the correlation of the interface roughness were studied by means of small angle X-Ray diffuse and specular reflection measurements. The specular reflection measurements provide information on the thickness, density and roughness of the layers. The diffuse reflection is particularly suited for determining the roughness correlation between layers in junction structures.

4.3 Experimental Results and Discussion

As the Fe₃O₄ layer is the base layer in the MgO (100)/Fe₃O₄/MgO/Fe stack structure, a high quality epitaxial growth of this layer is essential to the growth of subsequent layers. Thus, prior to the growth of the epitaxial thin film stack structure, the growth of Fe₃O₄ film on MgO (100) substrate was investigated by means of RHEED and HRXRD. The stoichiometry of the Fe₃O₄ film was characterized by the Verwey transition temperature obtained from the resistance-temperature (R-T) curve. The stoichiometry of Fe₃O₄ is sensitive to the Verwey transition temperature [44]. Here we focus on the HRXRD and R-T curve results, the RHEED result will be discussed later.

The (004) symmetric rocking curves of magnetite films grown on MgO substrate with a thickness of 100 nm are shown in figure 4.1, below. The out-of-plane and in-plane lattice parameters of the Fe₃O₄ film were calculated as 8.3604 ± 0.0005 and 8.4268 ± 0.0005 Å, respectively. The in-plane lattice parameter of the film is twice that of the MgO substrate, which is indicative of the mis-match (0.3%) relationship between Fe₃O₄ and MgO. To measure the in-plane lattice parameter a Reciprocal Space Map (RSM) near the asymmetric (226) reflection of the Fe₃O₄ film was obtained by carrying out several $\omega - 2\theta$ scans for different values of ω ($-0.5 - 0.5^\circ$). A contour plot of the intensity as a function of the in-plane and the out-of-plane reciprocal wave vectors, $Q(x)$ and $Q(z)$, for the Fe₃O₄ film is shown in figure 4.2. $Q(x)$ of the magnetite film is equal to that of the MgO substrate which indicates that the in-plane lattice parameters of the substrate and film are equal. Our results suggest that the magnetite films are epitaxial and remain in a fully strained state, coherent with the MgO substrate. The magnetite film grown on the MgO (100) substrate exhibits an out-of-plane compression strain and a corresponding in-plane tension.

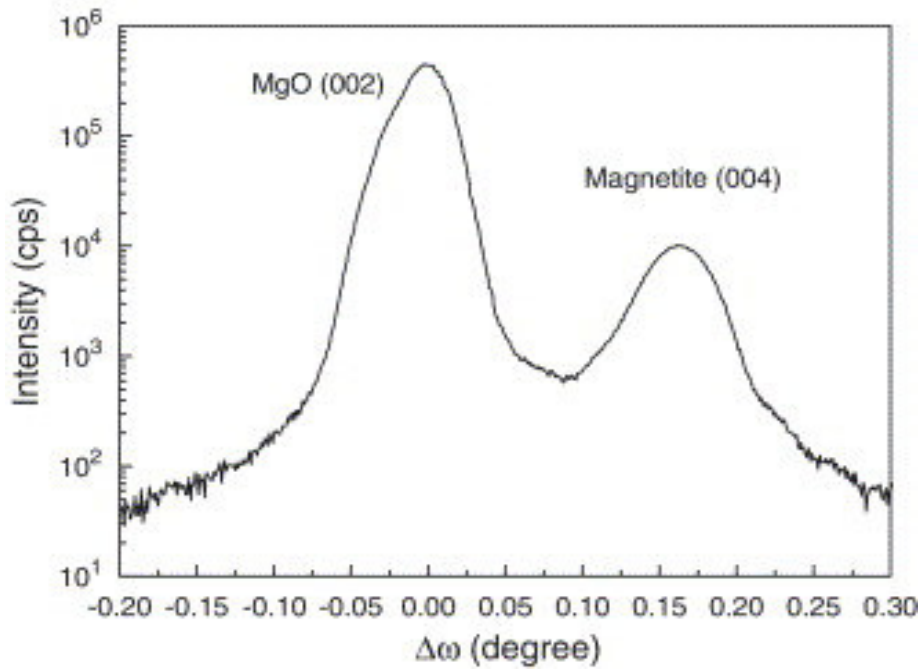


Figure 4.1: X-Ray diffraction rocking curve for the symmetric (004) peak of the Fe₃O₄ film. The higher intensity peak is the (002) peak of the MgO (100) substrate

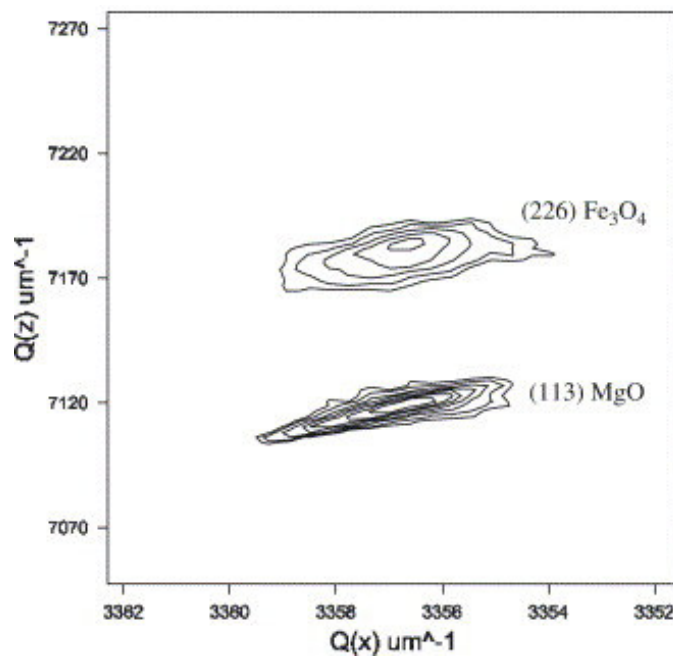


Figure 4.2: Reciprocal space map near the symmetric (226) glancing exit diffraction of the Fe₃O₄ film. The intense substrate (113) peak is also visible

The temperature dependence of resistance of the Fe₃O₄ film is shown in figure 4.3. The resistance increases greatly with decreasing temperature, as expected. The Verwey transition can be readily observed at ~115 K. This value is lower than the Verwey transition temperature (T_V) for bulk magnetite (120 K) but this is as expected as there is a trend towards a lower Verwey transition temperature for decreasing film thickness [45, 46]. The fact that the Verwey transition, which is very sensitive to the stoichiometry, is clearly observed in the R-T curve demonstrates that the film is very close to the ideal magnetite stoichiometry.

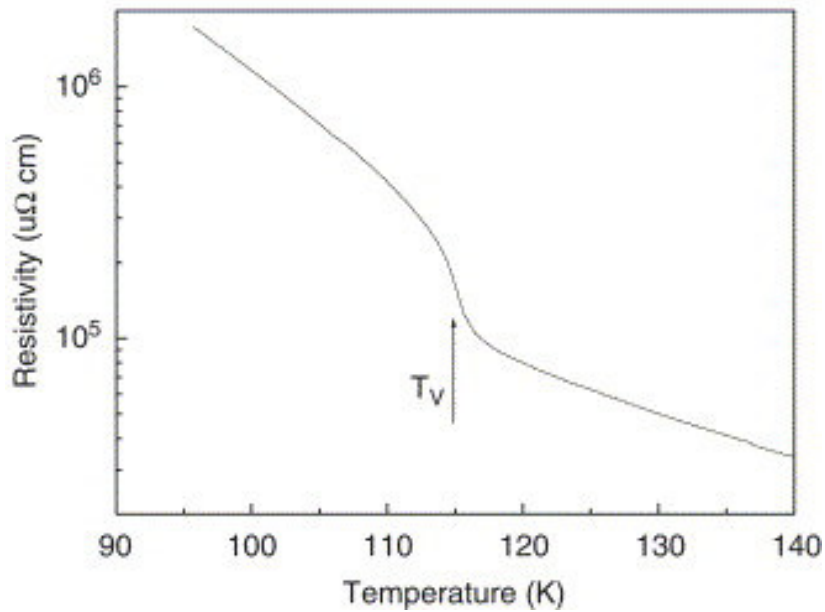


Figure 4.3: Resistivity of the Fe₃O₄ film as a function of temperature

RHEED patterns were used to monitor the epitaxial growth of the Fe₃O₄/MgO/Fe stack structures on the MgO (100) substrate. The representative patterns are shown in figure 4.4. Figure 4.4a shows the RHEED pattern of an MgO (100) substrate. The diffraction pattern shows the vertical surface lattice rods and parabolic Kikuchi lines, indicative of a smooth and ordered surface. Figure 4.4b is the RHEED pattern after the growth of a 15 nm thick Fe₃O₄ film. The half-order lattice rods are located in positions halfway between the locations of the MgO (100) lattice rods. This is indicative of the formation of epitaxial Fe₃O₄ and reflects the double periodicity of the unit cell of Fe₃O₄ compared to MgO. Figure 4.4c shows the re-establishment of the MgO (100) pattern as seen in figure 4.4a during the growth of the MgO

spacer layer. The thickness of the MgO layer in figure 4.4c is 0.95 nm. Figure 4.4d shows the vertical lattice rods associated with the epitaxial growth of Fe with a thickness of 10 nm on the MgO spacer layer. Figure 4.4e shows the RHEED pattern after the growth of a 25 nm Au layer on the Fe layer. The diffraction rods indicate that Au layer still grows epitaxial on the Fe layer. The RHEED images demonstrate that heteroepitaxial Fe₃O₄/MgO/Fe stack structures on MgO (100) substrate were obtained.

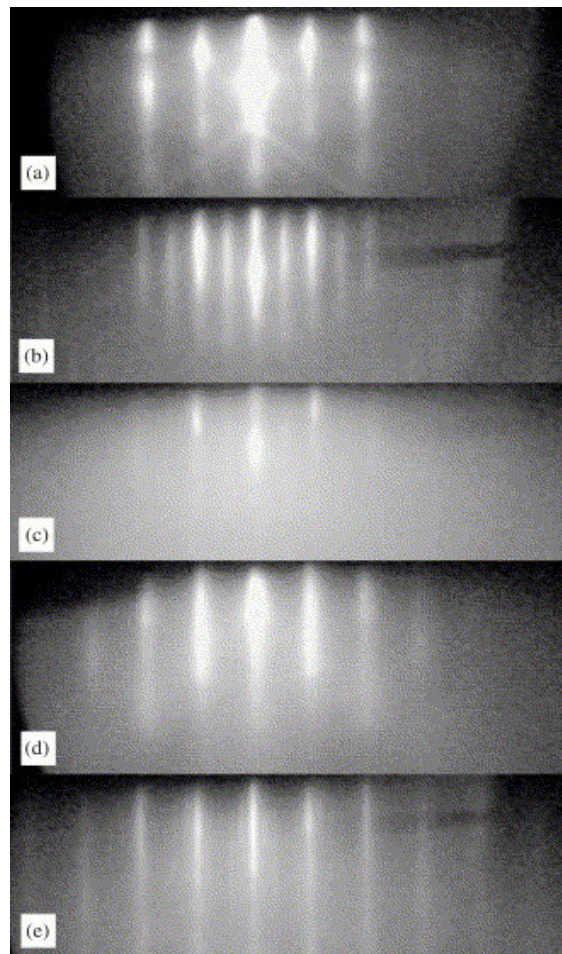


Figure 4.4: RHEED images of (a) a cleaned MgO (100) substrate, (b) after the growth of the 15 nm thick Fe₃O₄ bottom electrode, (c) after the growth of the 0.95 nm thick MgO barrier layer, (d) after the growth of the 10 nm thick Fe top electrode, and (e) after the growth of the 25 nm thick Au cap layer. All images were recorded along the $\langle 110 \rangle$ azimuth of the MgO substrate at electron beam energy of 20 kV

The interface roughness correlation in the stack structure was investigated by means of an X-ray reflection technique. The specular reflection patterns of the stack structures are shown in figure 4.5, where the MgO layer thickness is 0.95 nm (sample 1) and 2.0 nm (sample 2) respectively. By fitting theoretical expressions using Bede RFD Mercury v3.50b software, we derived the parameters listed in Table 4.1. The reflectivity curve of sample 1 exhibits more pronounced oscillations compared to that of sample 2. The roughness of the MgO layer in sample 1 is smaller than that in sample 2. A series of diffuse reflection scans with different offset angles from the specular condition were carried out. The specular, as well as diffuse X-ray reflections are shown in figure 4.6 (a) and (b) in the form of a contour map. The stretch of the scattering peak was clearly observed for sample 1 (figure 4.6a). On the contrary, no clear peak stretch was found for sample 2 (figure 4.6b). The stretch of the scattering peak arises from a high degree of roughness correlation between successive interfaces [47-49]. The incident X-rays can interfere with periodic multilayer even if the incident angle does not fulfill the Bragg condition. The results demonstrate that an interface roughness correlation exists for the MgO layer thickness of about 1 nm and disappears when the MgO layer thickness is some 2 nm. This suggests that a change in the growth mode of the MgO layer occurs in this thickness range. Initially the MgO film grows in a 2D mode and then at greater thickness it switches into the 3D mode because of the higher surface energy of MgO compared to that of Fe₃O₄. The observed results also suggest that there is no roughness correlation between the following layers after the MgO layer. This could be related to the partial shadowing of the flux by the MgO islands during the growth of the following layers.

Our results suggest that the interface roughness correlation across the MgO dielectric layer grown on Fe₃O₄ depends significantly on the layer thickness in the thickness range that is of interest for the growth of magnetic tunnel junctions. This needs to be taken into account in the interpretation of the dependency of the tunnel magnetoresistance on the thickness of the dielectric layer. The future study focusing on the effect of the correlation of layer interface roughness on the magnetic and transport properties of the junction is in progress.

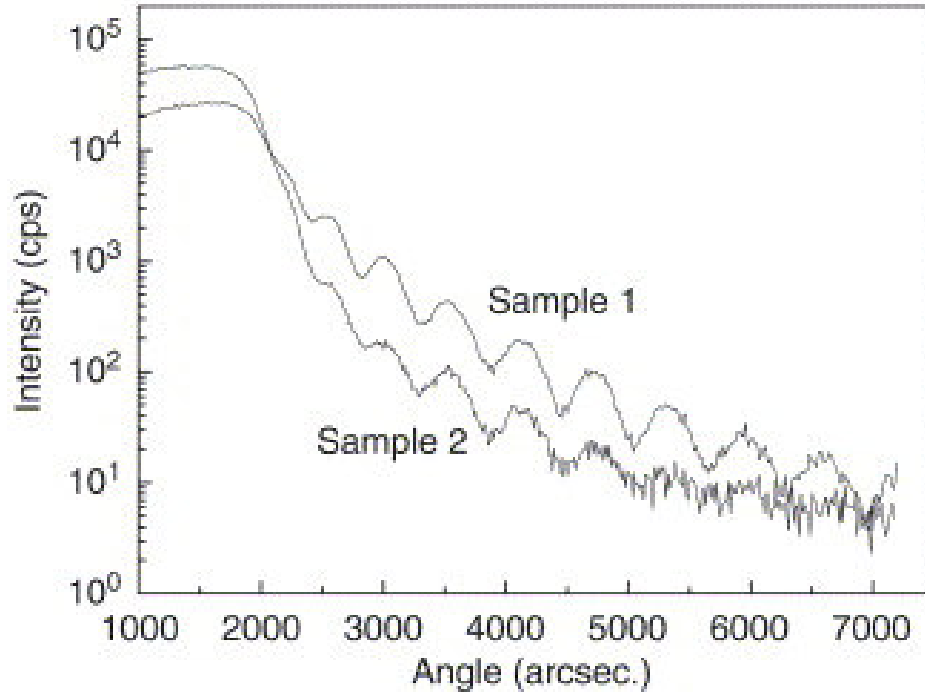


Figure 4.5: The spectral X-Ray reflectivity of sample 1 (0.95 nm thick MgO barrier layer) and sample 2 (2 nm thick MgO barrier layer)

Layer)	Roughness (nm) Sample 1 (0.95 nm thick MgO layer)	Roughness (nm) Sample 2 (2.0 nm thick MgO layer)
MgO substrate	0.801	1.649
Fe ₃ O ₄	0.440	0.557
MgO	0.649	0.975
Fe	0.308	0.374

Table 4.1: Roughness derived from the specular reflectivity curve

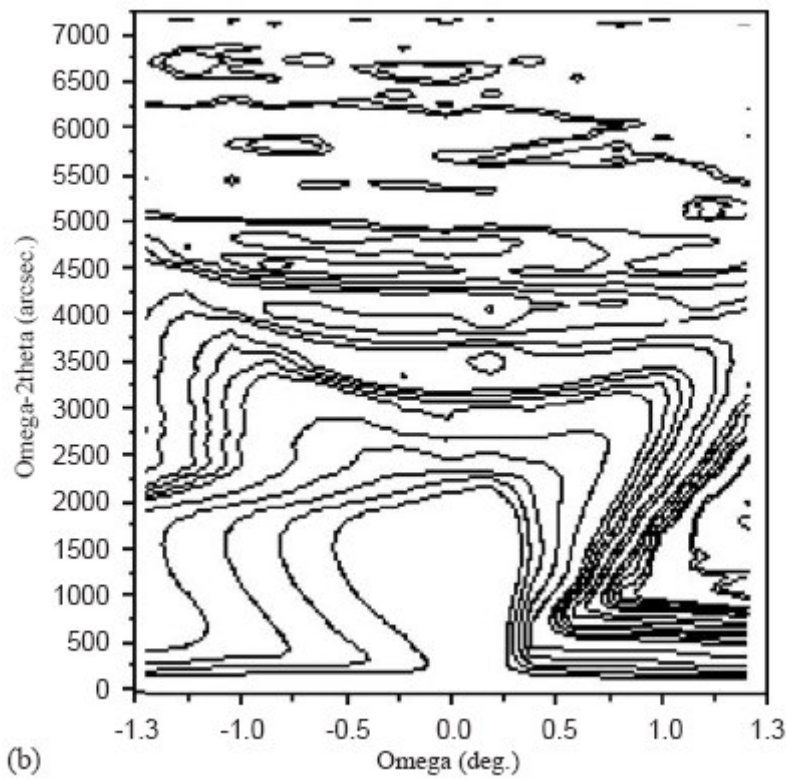
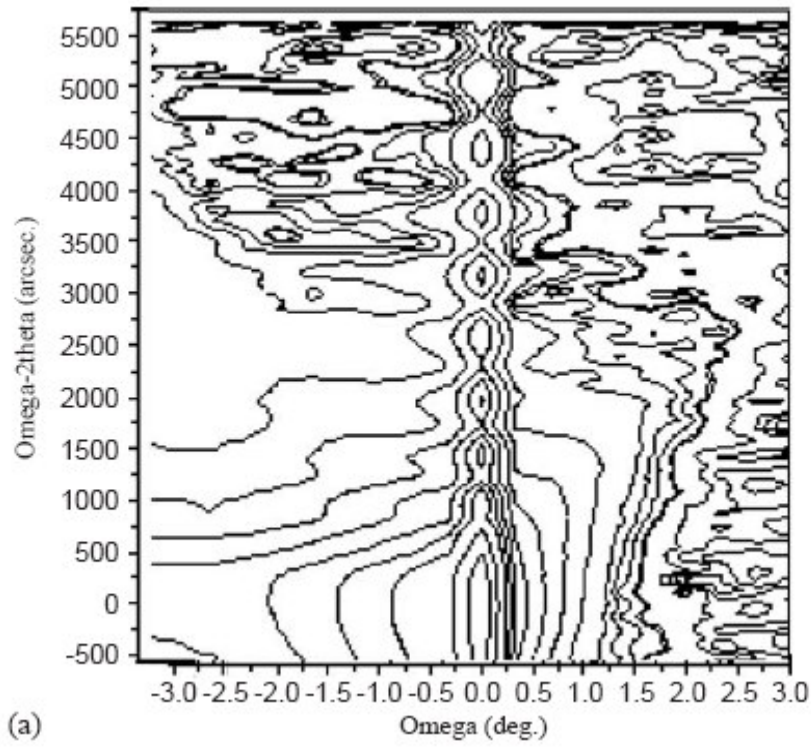


Figure 4.6: X-Ray reflectivity reciprocal space map of (a) sample 1 and (b) sample 2

4.4 Conclusion

The growth and interface roughness correlation between layer interfaces in Fe₃O₄/MgO/Fe stacks was investigated. Fe₃O₄/MgO/Fe stack structures were grown epitaxially on MgO (100) substrates. The Fe₃O₄ films were in a strained state, maintaining full coherence with the substrate. The correlation of the layer interface roughness existed when the thickness of the MgO layer was smaller than 1 nm. There were no traces of layer interface roughness correlation in the Fe₃O₄/MgO/Fe stack structure when the MgO layer was thicker than 2 nm. The change in the interface roughness correlation for the stack structure is thought to result from a change of the growth mode of the MgO layer. Initially the MgO film grows in a 2D mode and then at greater thickness it turns into the 3D mode. The results suggest that the correlation of interface roughness may take a role on the thickness dependence of MgO insulating layer on the electrical properties of tunneling junctions.

From this investigation we can conclude that MgO appears to be a suitable candidate as the insulating barrier layer for use in magnetic tunnel junctions. There are many more investigations necessary before a definite conclusion may be drawn regarding the suitability of MgO, these include an investigation into the role the barrier plays in the operation of a MTJ, the reproducibility of the growth of the epitaxial MgO, the quality of the MgO barrier layer in regards to surface coverage e.g. pinholes and the magnetoresistance obtainable from MTJs using MgO as the insulating barrier layer. This last point appears to have been answered by Parkin *et al* [13] and Yuasa *et al* [14] who have achieved a MR of 180% at room temperature for a MTJ using MgO as the insulating barrier layer.

Chapter 5: Fe₃O₄/MgO/Cr Epitaxial Thin Film Stack

5.1 Introduction

In this chapter we shall discuss the results of the MR measurements made on a (30 nm) Fe₃O₄ (100) / (x nm) MgO (100) / (5 nm) Cr (100) structure, where $1 < x < 6$ nm and a (5 nm) MgO (100) / (5 nm) Cr (100) structure. We shall also present HRXRD and Four Probe Resistivity measurements for a MgO (100) / (30 nm) Fe₃O₄ bilayer system to demonstrate that the magnetite film we are capable of depositing are of a very high quality. Each of these structures is essential because in investigating magnetic tunnel junction structures it is vital that each layer of the structure is fully characterised. Each structure was grown on MgO (100) single crystal substrates using molecular beam epitaxy. The proximity influence of the Fe₃O₄ bottom layer on the in-plane transport and magnetotransport properties of the Cr electrode was studied. It was hoped that this work would provide some information into the role of the MgO barrier layer on the operation of a magnetic tunnel junction. In fact a reversal of the magnetoresistance (MR) sign in the Cr film was observed for MgO layer thickness ≤ 5 nm. The thickness of the MgO layer at which the proximity influence of the Fe₃O₄ on the MR of the Cr layer is still observed is too large to be accounted for by an exchange interaction. Our results suggest that the magnetic structure in the Cr electrode adjoining a pinhole in the MgO barrier layer is distorted due to the exchange coupling. Such areas in the Cr film are thought to contribute to the negative MR. While pinholes in the barrier layer was not the result we were hoping for the fact that a reasonable explanation of the observed results was forthcoming is in itself quite satisfactory. It does however bring into doubt the suitability of MgO as grown under our conditions for use in a magnetic tunnel junction, where the only conduction path is supposed to be through the independent spin conduction channels.

The motivation behind this research was to add to the body of knowledge regarding the role of the barrier layer in the operation of a magnetic tunnel junction. To fully understand the role of MgO as a dielectric in tunnel junctions the magnetic interlayer coupling between the FM electrodes across the MgO layer must be understood. To this end the following systems were investigated:

- MgO (100) / (30 nm Fe₃O₄)
- MgO (100) / (30 nm) Fe₃O₄ / MgO (x nm) / (5 nm) Cr, (1<x<6 nm)
- MgO (100) / (5 nm) MgO / (5 nm) Cr

All three structures were grown on MgO (100) single crystal substrates. Magnetite (Fe₃O₄) was chosen not only due of it's already alluded to 100% spin polarisation but also because it is an interesting half-metallic ferromagnet whose resistivity is highly temperature dependent. This makes it possible to investigate the effect of the interlayer coupling on the transport properties of the Cr electrode when no current flows through the bottom electrode at low temperature.

The Cr film was chosen for the top electrode because of its low MR value. Studies have been reported on the magnetic structure of epitaxial Cr films, as mentioned in a previous chapter. Many of these studies were initiated some years ago due to interest in Fe/Cr multilayers and superlattices. As explained previously, epitaxial thin films of Cr, with a thickness of less than 10 nm, exhibit commensurate antiferromagnetic characteristics [30 - 33]. The expectation was that any influence of the bottom electrode (Fe₃O₄) on the top Cr electrode through the nonmagnetic MgO barrier layer would be readily observable.

5.2 Structure Growth and Characterisation

The structures used throughout this research were grown on MgO (100) single crystal substrates using Oxygen-Plasma-Assisted Molecular Beam Epitaxy (MBE). Full details regarding the deposition system and substrate annealing procedure are given in the Experimental Details chapter. The miscut angle of the MgO (100) substrate was less than 0.2°.

Briefly, the growth conditions for the various layers and electrodes under discussion were as follows: The Fe₃O₄ layer was deposited by means of electron gun evaporation from Fe

pellets with a purity of 99.995% in a plasma oxygen environment of 1×10^{-5} Torr at a substrate temperature (T_s) of 250 °C. The MgO layer was deposited from MgO pellets of 99.9% purity under similar conditions at a substrate temperature of 400 °C. The Cr film was deposited from Cr pellets of purity 99.995% in a vacuum of 5×10^{-8} Torr and a substrate temperature of 250 °C. The deposition rates were 0.3, 0.02 and 0.1 Å/s, respectively. The low growth rate for MgO and Cr were to promote epitaxial growth. The value 0.02 Å/s was arrived at after several attempts to grow epitaxial MgO. The growth rates were monitored and controlled using an INFICON IC-5 process controller and quartz thickness monitors.

The structure of the epitaxial thin films was characterised by means of High Resolution X-Ray Diffraction (HRXRD) using a Bede D1 system as described in the Experimental Details chapter. The correlation of the interface roughness was studied by means of an X-Ray reflection technique. The transport and magnetotransport properties were investigated using a four probe method, also described in the Experimental Details chapter. In all of the experiments outlined above the current was driven in the plane of the film through electrodes attached by means of a conducting epoxy. An external magnetic field of up to ~ 1500 kA/m was applied in the plane of the thin film and parallel to the applied current, which is along the (110) direction of the Cr film. The current was supplied by a lock-in-amplifier (Stanford Research System SR 830), which was also used for measurement purposes. An AC current (74 μ A) with a frequency of 187 Hz was employed in this work.

5.3 Experimental Results

In situ reflection high energy electron diffraction (RHEED) patterns were used to monitor the epitaxial growth of the structures. Figure 5.1 shows the RHEED patterns achieved during the growth of the layers that constitute the epitaxial thin film stacks under discussion. Figure 5.1 (a) shows the RHEED pattern of an MgO (100) substrate. The diffraction pattern shows the vertical surface lattice rods and parabolic Kikuchi lines, indicative of a clean, smooth and well ordered surface. Figure 5.1 (b) shows the half-order lattice rods, located in positions halfway between the locations of the MgO (100) lattice rods. This is indicative of the formation of epitaxial Fe₃O₄ and reflects the double periodicity of the unit cell of Fe₃O₄ compared to MgO.

Figure 5.1 (c) shows the reformation of the MgO (100) pattern, as seen in figure 5.1 (a), during the growth of the MgO barrier layer. Finally, figure 5.1 (d) shows the vertical lattice rods associated with the epitaxial growth of the Cr top layer/electrode on the MgO barrier layer. The RHEED images demonstrate that heteroepitaxial MgO (100) / Fe₃O₄ (100) / MgO (100) / Cr (100) structures were obtained. While these RHEED patterns were obtained during the growth of one of the epitaxial thin film stacks structures under investigation they are indicative of the RHEED patterns achieved for all the structures grown. This means that figures 5.1 (a) and 5.1 (b) are representative of the MgO (100) / MgO / Cr structure and the MgO (100) / Fe₃O₄ structure while figures 5.1 (c) and 5.1 (d) are representative of the MgO (100) / Fe₃O₄ / MgO / Cr structure and the MgO (100) / MgO / Cr structure. This is further proof of the heteroepitaxial nature of the structures obtained, seeing as each individual layer grew epitaxially.

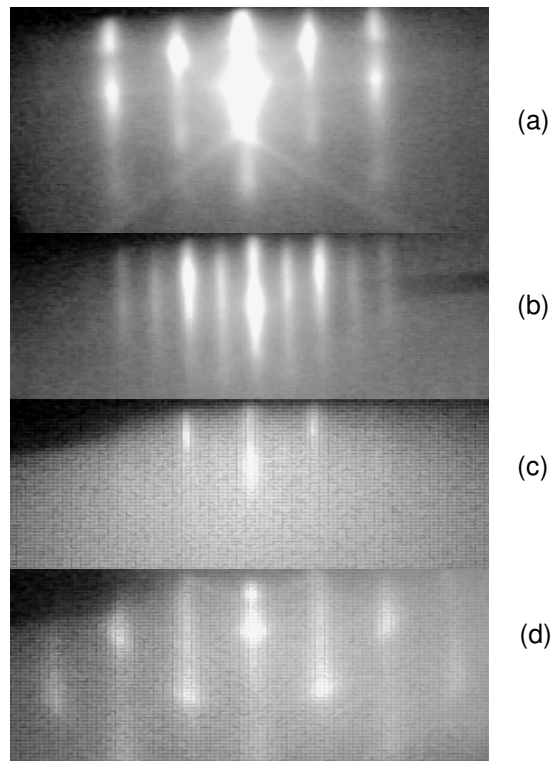


Figure 5.1: RHEED images of (a) cleaned MgO (100) substrate, (b) after growth of the 30 nm thick Fe₃O₄ bottom electrode, (c) after growth of the 1 nm MgO insulating barrier layer, and (d) after the growth of the 5 nm Cr top electrode. All images were recorded along the $\langle 110 \rangle$ azimuth at an electron beam energy of 20 kV.

Figure 5.2 shows the X-Ray rocking curve for the Fe₃O₄ /MgO (100) structure for the symmetric (004) and asymmetric (226) peaks. From the separation of the diffraction peaks it was calculated that the in-plane magnetite lattice parameter, a_{\parallel} , was 0.8426 nm and the out-of-plane magnetite lattice parameter, a_{\perp} , was 0.8360 nm. The in-plane magnetite lattice parameter, a_{\parallel} , was exactly twice that of the MgO lattice parameter (0.4213 nm). This indicates the magnetite film grown on the MgO (100) substrate exhibits an out-of-plane compressive strain and a corresponding in-plane tensile strain and that the film was in a fully strained state. It also demonstrates that the magnetite grew epitaxially on the MgO (100) substrate further proving that heteroepitaxial structures were obtained.

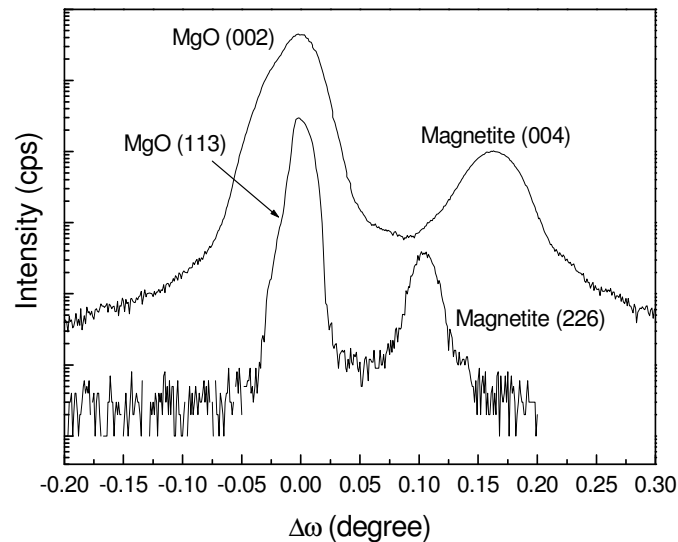


Figure 5.2: X-Ray diffraction rocking curve for the symmetric (004) and asymmetric (226) peaks for the 30 nm thick magnetite film. The higher intensity peaks are the (002) and the (113) peaks of the MgO (100) substrate

Figure 5.3 shows the resistivity and magnetoresistance, at a field of 1500 kA/m, of the (30 nm) Fe₃O₄ structure on a single crystal MgO (100) substrate as a function of temperature. In this instance the magnetoresistance is defined as $[R(H) - R(0)]/R(0)$. The resistance of the magnetite film increases greatly with decreasing temperature, as expected. The Verwey transition can be easily observed at ~115 K. This value is lower than the Verwey transition

temperature for bulk magnetite (~120 K) but this is as expected as there is a trend towards a lower Verwey transition temperature for decreasing film thickness [45, 46]. As the Verwey transition is sensitive to stoichiometry, its presence in the film demonstrates that the magnetite film under investigation is close to the ideal magnetite stoichiometry. Figure 5.3 also shows that the magnetite film displays a negative MR value. The MR of the magnetite film increases with decreasing temperature. Ziese and Blythe [50] have reported a detailed investigation of the magnetoresistance of single crystal and thin film magnetite.

In this study we focus on the influence of the magnetoresistance of the Cr film caused by the ferromagnetic electrode across a nonmagnetic insulating MgO barrier layer. It was realised that the MR of the Cr layer might be affected by the possible formation of an alloy caused by interdiffusion at the Cr-MgO interface. To exclude this possibility comparable studies were performed on the following systems: MgO (100) / (5 nm) MgO / (5 nm) Cr and MgO (100) / (30 nm) Fe₃O₄ / (5 nm) MgO (5 nm) Cr . The two systems were grown under identical conditions at the same MgO (100) substrate temperature and deposition rate. Representative RHEED images can be seen in figure 5.1. Representative results for the transport and magnetotransport properties of the Cr film in the structure MgO (100) / (5 nm) MgO / (5 nm) Cr are shown in figure 5.4. It was found that the resistivity of the Cr film decreased with decreasing temperature, indicative of metallic behaviour. In contrast to the reported value for bulk Cr crystals, a positive MR for the Cr film was observed. Abdul-Razzaq and Amoruso [29] reported that a positive MR had been observed for a Cr film with a thickness of 30 nm, in agreement with this present work. These results lead to the conclusion that there is no interdiffusion at the Cr-MgO interface.

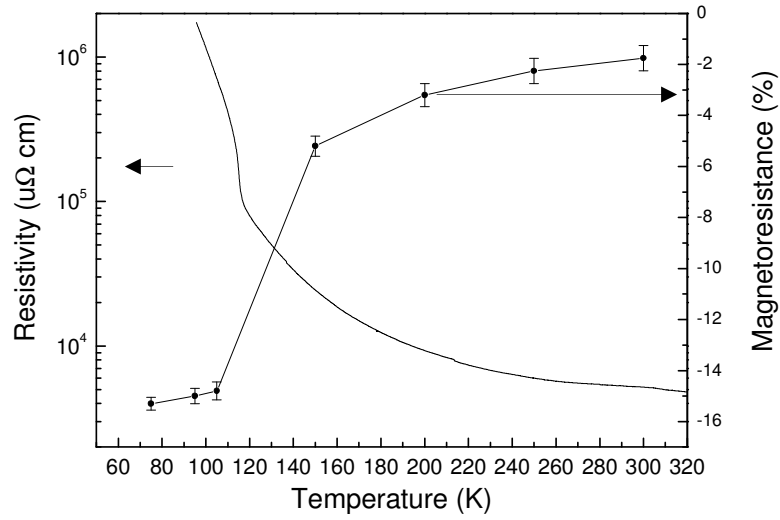


Figure 5.3: Resistivity and magnetoresistivity at a 1500 kA/m field of the 30 nm magnetite film as a function of temperature. The line joining the magnetoresistance data points is added as a guide for the eye

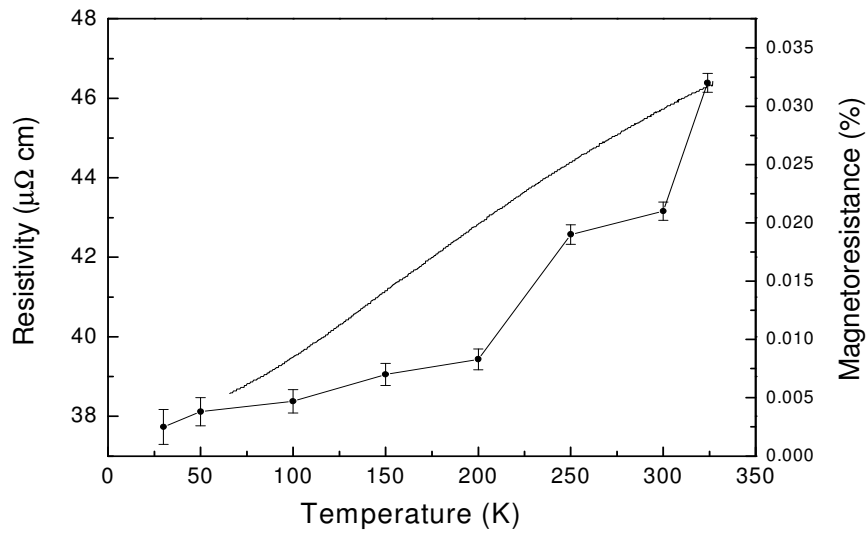


Figure 5.4: Resistivity and magnetoresistivity at a 1500 kA/m field of the 5 nm Cr film as a function of temperature. The line joining the magnetoresistance data points is added as a guide for the eye

Figure 5.5 shows the dependence of the MR at a field of 1500 kA/m on the MgO barrier layer thickness at 30 K for the MgO (100) / (30 nm) Fe₃O₄ / (1-6 nm) MgO / (5 nm) Cr stack structure. This is the central result of this chapter. In contrast to the positive MR for the MgO (100) / (5 nm) MgO / (5 nm) Cr stack structure, a negative MR was observed for the MgO (100) / (30 nm) Fe₃O₄ / (x nm) MgO / (5 nm) Cr stack structure for an MgO layer less than 5 nm thick ($\tau_{\text{MgO}} \leq 5$ nm). A positive MR, coinciding with the one observed for the MgO (100) / (5 nm) MgO / (5 nm) Cr stack structure, was only observed for $\tau_{\text{MgO}} > 5$ nm. This implies that the influence of the Fe₃O₄ electrode on the MR of the Cr electrode exists for values for $\tau_{\text{MgO}} \leq 5$ nm and vanishes for values of $\tau_{\text{MgO}} > 5$ nm. The MR of the MgO (100) / Fe₃O₄ / MgO / Cr stack structure was linear for a field up to 1500 kA/m, which was the maximum field available for this work. It seems remarkable that the influence of the Fe₃O₄ ferromagnetic bottom electrode on the MR of the Cr electrode extends across such a thick MgO barrier layer. While this was not the desired result it was the observed result and therefore needs explanation.

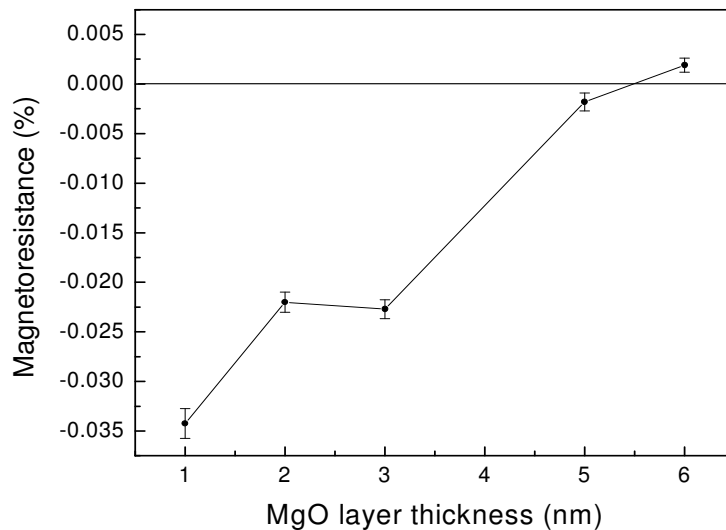


Figure 5.5: Dependence of the magnetoresistance of the MgO (100) / (30 nm) Fe₃O₄ / (1-6 nm) MgO / ((5 nm) Cr structure at a field strength of 1500 kA/m and a temperature of 30 K.

5.4 Discussion

In this section we shall discuss the possible mechanisms responsible for the surprisingly long range influence of the magnetite bottom electrode on the MR of the top Cr electrode. The

three mechanisms for consideration are (1) electrical bridging through possible pinholes in the MgO barrier layer, (2) magnetostatic coupling (“orange peel” coupling) and (3) direct magnetic coupling through the possible pinholes in the MgO barrier layer.

5.4.1 Electrical Bridging Through the Pinholes

Electrical bridging through the pinholes can be disregarded as a possible mechanism as it could not account for the observed negative MR for the MgO (100) / Fe₃O₄ / MgO / Cr stack structure. This can be understood by expressing the resistance of the Cr film and the magnetite substrate in the presence of a field H as $R_{Cr \text{ or } Fe_3O_4}(H, T) = R_{Cr \text{ or } Fe_3O_4} [1 + MR_{Cr \text{ or } Fe_3O_4}(H, T)]$, where $R_{Cr \text{ or } Fe_3O_4}$ is the resistance at zero field and $MR_{Cr \text{ or } Fe_3O_4}(H, T)$ is the magnetoresistance co-efficient of the Cr film and magnetite substrate, respectively, under the external magnetic field (H) at temperature (T).

Based on the model of two parallel resistors the MR of the entire film substrate system is:

$$MR_{f-s}(H) = \frac{MR_{Cr}(H, T)[1 + MR_{Fe_3O_4}(H, T)] + \frac{R_{Cr}}{R_{Fe_3O_4}} MR_{Fe_3O_4}(H, T)[1 + MR_{Cr}(H, T)]}{[1 + MR_{Fe_3O_4}(H, T)] + \frac{R_{Cr}}{R_{Fe_3O_4}} [1 + MR_{Cr}(H, T)]} \quad (5.1)$$

The results from this equation are graphed in figure 5.6 as a function of the ratio of the film to substrate resistances. The measured values of the MR of epitaxial magnetite and Cr were used for this calculation; these values were -15% and 0.0025% respectively. This clearly demonstrates that the MR of the film-substrate system is largely dependent on the MR of the Cr film provided that the ratio $R_{Cr}/R_{Fe_3O_4}$ is small. Typical resistance values for Cr film and magnetite, at 30 K, are 50 Ω and 500 k Ω , respectively. This implies a $R_{Cr}/R_{Fe_3O_4}$ ratio of $\sim 1 \times 10^{-4}$ which, from figure 5.6, should yield a positive MR. This is contrary to our experimental observations of a negative MR and thus it is concluded that electrical coupling through the pinholes does not play a significant role in the MR of the entire film-substrate system.

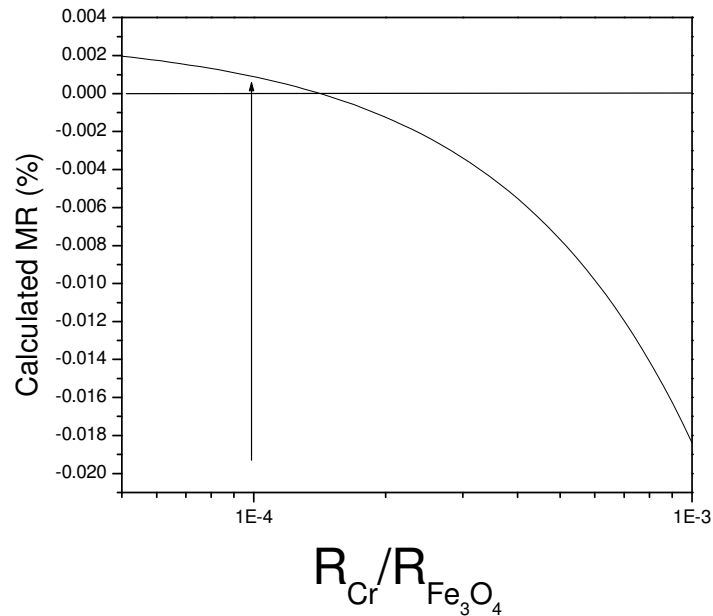


Figure 5.6: Calculated magnetoresistance of the Cr film – Fe₃O₄ electrode system as a function of film to substrate resistance ratio ($R_{Cr}/R_{Fe_3O_4}$). The line joining the magnetoresistance points is added as a guide for the eye.

5.4.2 Magnetostatic (“Orange Peel”) Coupling

Neel magnetostatic coupling, also referred to as “orange peel” coupling, results from the correlated interface roughness of the Cr film and magnetite surface. This mechanism has been extensively studied recently. The interlayer coupling between Fe₃O₄ layers separated by an MgO insulating barrier layer with thickness in the range 0 – 45 nm has been investigated [51]. Coupling for an MgO insulating barrier thicker than 1.3 nm was attributed to Neel magnetostatic coupling. The magnetic field due to Neel coupling depends on the surface roughness. The X-Ray reflectivity reciprocal space map of the MgO (100) / Fe₃O₄ / MgO / Cr stack structure, as shown in figure 5.7, clearly demonstrates that there is good interlayer correlation for the MgO (100) / Fe₃O₄ / MgO / Cr stack structure, structure. This is evidenced from the elongation of the peaks in the reciprocal space map. Such features are indicative of a good interlayer correlation [52, 53 and 54].

Therefore, the basic assumptions for the “orange peel” model were fulfilled for our structures. The coupling field H could be modelled assuming that the surface has a two dimensional sinusoidal waviness with amplitude h and wavelength ω [55].

$$H = \frac{\pi^2 h}{\sqrt{2} \omega} M_s \exp\left(-\frac{2\pi\sqrt{2}}{\omega} t\right) \quad (5.2)$$

where M_s is the saturation magnetisation of the substrate and t is the thickness of the nonmagnetic barrier layer. For demonstration purposes, the bulk saturation magnetisation for magnetite (470 kA/m) was used. Values for h and ω were determined from AFM measurements of the MgO (100) / Fe₃O₄ / MgO / Cr stack structure. These values thus determined were $h = 1.5$ nm and $\omega = 412$ nm.

Calculated values are tabulated in table 5.1 and demonstrate that the additional field created in the Cr film due to the magnetostatic coupling small in comparison to the 1500 kA/m field in which the MR of the MgO (100) / Fe₃O₄ / MgO / Cr stack was measured. Thus, it was concluded that the effect of the magnetostatic coupling cannot explain the reversal of the MR observed.

t (nm)	H (kA/m)
1	11.7
3	11.2
5	10.73

Table 5.1: Calculated coupling field based on the “orange peel” model

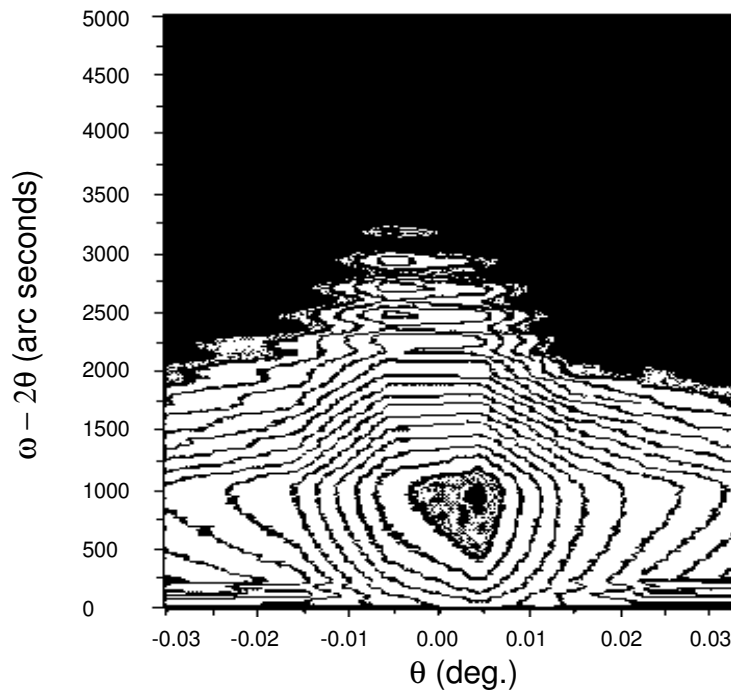


Figure 5.7: X-Ray reflectivity reciprocal space map for the structure: MgO (100) / (30 nm) Fe₃O₄ / (1 nm) MgO / (5 nm) Cr structure

5.4.3 Direct Magnetic Coupling through the Pinholes

The final mechanism to consider explaining the long range effect of the magnetite bottom electrode on the top Cr electrode is direct magnetic coupling through the pinholes. This is an extension of the idea applied to a similar polycrystalline trilayer system by Jin [56]. The model predicts that the magnetic structure in the Cr film in the direct vicinity of a pinhole is distorted through an exchange interaction with the bottom magnetite electrode. This is represented schematically in figure 5.8.

The distortion is affected and modified in the presence of an external magnetic field as the field rotates the magnetisation of the magnetite region, coupled through the pinhole to the Cr film. The model suggests that the electrons undergo less scattering in the regions of distorted magnetic structure, which explains the negative MR observed. Furthermore, it is suggested that the pinhole does not have to be completely open for the exchange interaction between the Cr film and the magnetite electrode to lead to a distorted magnetic structure in the Cr film.

This would explain the negative MR up to an MgO thickness of 5 nm, a thickness at which pinholes may not necessarily exist. Even when a pinhole is not completely open it is reasonable to expect that the Cr and magnetite regions simply need to be positioned in close enough proximity for the exchange interaction to become effective. This is shown schematically in figure 5.8 (c). It was proposed by Slonczewski [34] that pinholes are present in an MgO layer up to a thickness of ~3 nm when the insulating layer is deposited on an MnZn spinel substrate. More recent investigation by van der Heijden et al [51] indicates that pinholes exist for an MgO layer up to 1.3 nm thick. It is clear that the critical thickness above which pinholes no longer exist is dependent on the substrate strain status in the MgO film and on the growth conditions for the film. However, these values indicate that the exchange interaction between the Cr and magnetite is effective even when a 1-2 nm thick MgO insulating barrier layer separates them.

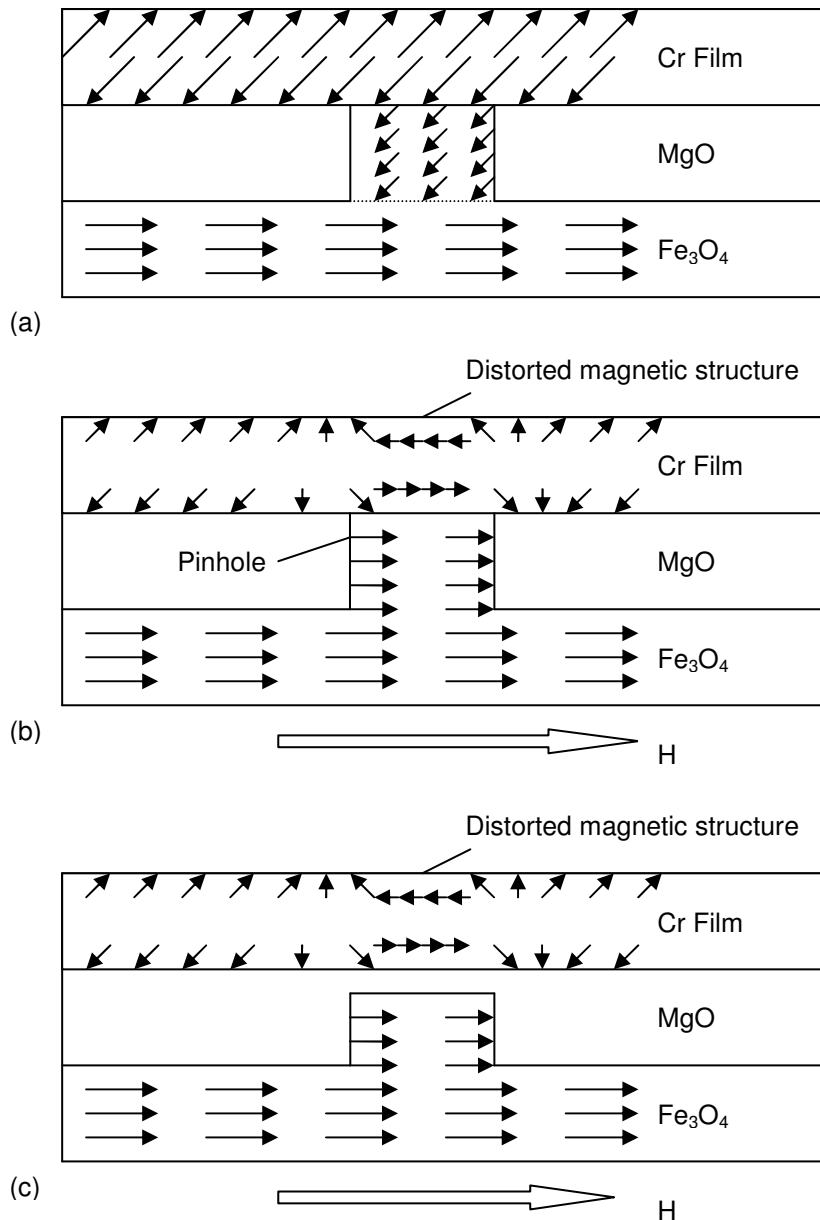


Figure 5.8: (a) Schematic diagram of a pinhole. The material in the pinhole forms a domain coupled to the Cr film by exchange interaction. The external field is zero. (b) External magnetic field is applied. This rotates the magnetic moments in the magnetite in the pinhole area and also spins in the Cr layer, which are coupled by exchange with the magnetite layer. This creates an area with a distorted magnetic structure where the electrons travelling in the Cr film undergo less scattering. (c) The case where a pinhole is not completely open, i.e. there is a thin layer of MgO preventing electric contact between the Cr and the magnetite substrate but still placing the two in close proximity.

5.5 Conclusion

The purpose of this investigation was to probe the role of the MgO insulating barrier layer on the operation of a magnetic tunnel junction. This was to be achieved by investigating the influence of the bottom magnetite electrode on the in-plane transport and magnetotransport properties of a top Cr electrode using a MgO (100) / (30 nm) Fe₃O₄ (100) / (1-7 nm) MgO (100) / (5 nm) Cr (100) epitaxial structure as well as a MgO (100) / 30 nm Fe₃O₄ (100) structure and a MgO (100) / (5 nm) MgO (100) / (5 nm) Cr (100) structure. All structures were grown on single crystal MgO (100) substrates. The experimental observations suggested that there were pinholes present in the MgO insulating barrier layer. This is thought not to be an ideal situation for MTJs and as such the growth conditions for the MgO insulating barrier layer will have to be modified to exclude the formation of pinholes in the MgO insulating barrier layer at a thickness of ~1 nm. One possible method for the formation of pinhole free MgO was presented by Yuasa *et al* [14].

Our experimental observations were that a distinct proximity influence of the bottom magnetite electrode on the top Cr electrode was observed when the thickness of the MgO insulating barrier layer was less than 5 nm. The influence was so extreme that the sign of the MR was reversed, resulting in a negative MR for the Cr electrode. The effects of electrical coupling through the pinholes and Neel magnetostatic coupling were excluded as possible mechanisms for the observed negative MR. The model of direct magnetic coupling through the pinholes for such systems appears to be verified by the observed results.

6: Conclusion:

Two Fe_3O_4 / MgO based magnetic tunnel junctions systems were investigated to determine the role the MgO barrier layer plays in their operation.

The first investigation centred on the fabrication of a Fe_3O_4 / MgO / Fe on MgO (100) magnetic tunnel junction with the aim to determine whether an epitaxial structure could be formed. To this end we investigated, through HRXRD methods, the interlayer roughness and the interlayer correlation between the layers of the junctions. We determined that the Fe_3O_4 film was in a fully strained state and maintained full coherence with the substrate. A correlation of interface roughness existed when the thickness of the MgO barrier layer was less than 1 nm. There was no indication of a layer interface roughness correlation for MgO barrier layers thicker than 2 nm. The change in the interface roughness correlation for the junction structures was thought to originate from a change in the growth mode of the MgO layer. Initially it is thought that the MgO layer grew in a 2D mode, but at greater thickness the growth mode changed to 3D. Our investigation of this system indicates that the correlation of interface roughness may play a significant role in the operation of magnetic tunnel junctions. At the very least we have demonstrated that epitaxial magnetic tunnel junctions based on MgO and Fe_3O_4 are feasible.

Our investigation of the Fe_3O_4 / MgO / Cr on MgO (100) system revealed interesting results, for which an explanation was presented. We investigated the influence of the magnetite bottom layer on the MR of the Cr layer by using two similar systems, a MgO (100) / (30 nm) Fe_3O_4 (100) / (1 - 6 nm) MgO (100) / (5 nm) Cr (100) epitaxial structure as well as a MgO(100) / (5 nm) MgO / (5 nm) Cr epitaxial structure. A distinct proximity influence of the magnetite on the Cr layer was observed for MgO barrier layer thickness less than 5 nm. The influence was such that the sign of the MR of the top Cr layer reversed, resulting in a negative MR for the Cr layer. The effects of electrical coupling through the pinholes and Neel magnetostatic coupling were excluded as possible mechanisms for the observed negative MR. A model of direct magnetic coupling through the pinholes for such systems appears to be verified by the observed results. While this may not have been the result that was

expected the fact that an explanation was forthcoming is somewhat reassuring. From this we can conclude that the MgO barrier layers grown under our conditions, while epitaxial in nature, may not be suitable for use in magnetic tunnel junctions. For tunnel junctions pinhole free barrier layers are required to ensure that the transport properties are dominated by tunnelling phenomena.

We have demonstrated that heteroepitaxial magnetic tunnel junction structures consisting of Fe_3O_4 and MgO are possible but that under our growth conditions their properties are not maximised. Thus, a refined growth procedure is required to rid the MgO barrier layer of pinholes. Such a refinement would be to grow the MgO barrier layer at the same rate but with a room temperature substrate temperature. This work is ongoing within the research group.

7 Bibliography:

- [1] M. Julliere, Phys. Lett. A, **54** (1975) 225
- [2] Meservey, P. M. Tedrow, P. Fulde, Phys. Rev. Lett., **25** (1970) 1270
- [3] R. Meservey, P. M. Tedrow, Phys. Rev. Lett., **26** (1971) 192
- [4] R. Meservey, P. M. Tedrow, Phys. Rep., **238** (1994) 173
- [5] Dana Borsa, Ph. D. Thesis, University of Groningen, Netherlands
- [6] J. S. Moodera, L. R. Kinder, T. M. Wong, R. Meservey, Phys. Rev. Lett., **74** (1995) 3273
- [7] W. J. Gallagher, S. S. P. Parkin, Yu. Lu, X. P. Bian, A. Marley, K. P. Roche, R. A. Altman, S. A. Rishton, C. Jahnes, T. M. Shaw, Gang Xiao, J. Appl. Phys., **81** (1997) 3741
- [8] M. Sato, K. Kobayashi, Jpn. J. Appl. Phys., Part 1 **36** (1997) 200
- [9] J. M. Daughton, J. Appl. Phys., **81** (1997) 3758
- [10] S. S. P. Parkin, K. P. Roche, M. G. Samant, P. M. Rice, R. B. Beyers, R. E. Scheuerlein, E. J. O'Sullivan, S. L. Brown, J. Bucchigano, D. W. Abraham, Yu. Lu, M. Rooks, P. L. Trouilloud, R. A. Wanner, W. J. Gallagher, J. Appl. Phys., **85** (1999) 5828
- [11] J. S. Moodera, J. Nowak, R. J. M. van de Veerdonk, Phys. Rev. Lett., **80** (1998) 2941
- [12] R. C. Sousa, J. J. Sun, V. Soares, P. P. Freitas, A. Kling, M. F. de Silva, J. C. Soares, J. Appl. Phys., **85** (1999) 5258
- [13] Stuart S. P. Parkin, Christian Kaiser, Alex Panchula, Philip M. Rice, Brian Hughes, Mahesh Samant, See-Hun Yang, Nature Materials **3(12)** (2004) 862
- [14] Shinji Yuasa, Taro Nagahama, Akio Fukushima, Yoshishige Suzuki and Koji Ando, Nature Materials **3(12)** (2004) 868
- [15] M. B. Stearns, J. Magn. Magn. Mater., **5** (1977) 167
- [16] S. F. Alvarado, W. Eib, F. Meier, D. T. Pierce, K. Sattler, H. C. Siegmann, J. P. Remeika, Phys. Rev. Lett., **34** (1975) 319

-
- [17] Xuesong Jin, Ciarán McEvoy, I. V. Shvets, *J. Magn. Magn. Mater.* **286** (2005) 128
- [18] Ciarán McEvoy, Xuesong Jin, I. V. Shvets, *J. Magn. Magn. Mater.* **283** (2004) 171
- [19] R. Scha, P. Belien, G. Verbanck, C. D. Potter, K. Temst, V. V. Moshchalkov, Y. Bruynseraede, *J. Magn. Magn. Mater.* **183** (1998) 65
- [20] E. Kunnen, K. Temst, V. V. Moshchalkov, Y. Bruynseraede, *Physics B* **276** (2000) 738
- [21] P. A. A. van der Heijden, M. G. van Opstal, C. H. W. Swuste, P. H. J. Bloemen, J. M. Gaines, W. J. M. de Jonge, *J. Magn. Magn. Mater.* **182** (1998) 71
- [22] P. Shah, M. Sohma, K. Kawaguchi, *J. Magn. Magn. Mater.* **247** (2002) 1
- [23] F. C. Voogt, T. M. M. Palstra, L. Niesen, O. C. Rogojanu, M. A. James, T. Hibma, *Phys. Rev. B*, **57** (1998) R8107
- [24] R. Moons, S. Blasser, J. Dkoster, A. Vantomme, J. De Wachter, G. Langouche, *Thin Solid Films* **324** (1998) 129
- [25] J. F. Lawler, R. Schad, S. Jordan, H. van Kempen, *J. Magn. Magn. Mater.*, **165** (1997) 224
- [26] J. S. Moodera, G. Mathon, *J. Magn. Magn. Mater.*, **200** (1999) 248
- [27] Wilma Eerenstein, Ph. D. Thesis, University of Groningen, Netherlands (2004)
- [28] E. W. J. Verwey, *Nature*, **144** (1937) 327
- [29] W. Abdul-Razzaq, M. Amoruso, *Physics B*, **253** (1998) 47
- [30] Hartmut Zabel, Patrick Bodeker, Andreas Schreyer, *J. Phys. D: Appl. Phys.*, **31** (1998) 656
- [31] E. E. Fullerton, S. D. Bader, J. L. Robertson, *Phys. Rev. Lett.*, **77** (1996) 1382
- [32] E. E. Fullerton, A. Adenwalla, G. P. Felcher, K. T. Riggs, C. H. Sowers, S. D. Bader, J. L. Robertson *Physica B*, **221** (1996) 370
- [33] A. Schreyer, C. F. Majkrzak, Th. Zeidler, T. Schmitte, P. Bodeker, K. Theis-Brohl, A. Abromeit, J. A. Dura, T. Watanabe, *Phys. Rev. Lett.*, **79** (1997) 4914
- [34] J. Slonczewski, *Phys. Rev. B*, **39** (1989) 6995

-
- [35] W. Braun, Applied RHEED – Reflection High Energy Diffraction During Crystal Growth, Springer Tracts in Modern Physics Volume 154 (1999)
- [36] J. Faure-Vincent, C. Tiusan, C. Bellouard, E. Popova, M. Hehn, F. Montaigne, A. Schuhl, Phys. Rev. Lett., **89** (2002) 107206
- [37] M. Przybylski, J. Grabowski, F. Zavaliche, W. Wulfhekel, R. Scholz, J. Kirschner, J. Phys. D – Appl. Phys., **35** (2002) 1821
- [38] J. Mathon, A. Umerski, Phys. Rev. B, **63** (2001) 220403
- [39] E. Bertel, N. Memmel, Appl. Phys. A, **63** (1996) 523
- [40] S. K. Sinha, E. B. Sirota, S. Garoff, H. B. Stanley, Phys. Rev. B, **38** (1988) 2297
- [41] S. A. Stepanov, E. A. Kondrashkina, R. Kohler, D. V. Novikov, G. Materlik, S. M. Durbin, Phys. Rev. B, **57** (1998) 4829
- [42] B. L. Peterson, R. L. White, B. M. Clemens, Physica B, **336** (2003) 157
- [43] M. Coey, Nature Materials, **4** (2005) 9
- [44] J. P. Shepherd, J. W. Koenitzer, R. Aragon, J. Spalek, J. M. Honig, Phys. Rev. B, **43** (1991) 8461
- [45] S. P. Sena, R. A. Lindley, H. J. Blythe, Ch. Sauer, M. Al-Kafarji, G. A. Gehring, J. Magn. Magn. Mater., **176** (1997) 111
- [46] G. Q. Gong, A. Gupta, Gang Xiao, W. Qian, V. P. Dravid, Phys. Rev. B, **56** (1997) 5096
- [47] A. J. G. Leenaers, J. J. A. M. Vrakking, D. K. G. de Boer, Spectrochim Acta B, **52** (1997) 805
- [48] K. N. Stoev, K. Sakurai, Spectrochim Acta B, **54** (1999) 41
- [49] I. Busch, J. Stumpel, Appl. Surf. Sci., **212-213** (2003) 201
- [50] M. Ziese, H. J. Blythe, J. Phys.: Condens. Matter, **12** (2000) 13
- [51] P. A. A. van der Heijden, P. J. H. Bloemen, J. M. Metselaar, R. M. Wolf, J. M. Gaines, J. T. W. M. van Eemeren, P. J. Van der Zaag, W. J. M. de Jonge, Phys. Rev. B, **49** (1997) 11569
- [52] V. Holy, T. Baumbach, Phys. Rev. B, **49** (1994) 10668
- [53] V. M. Kaganer, S. A. Stepanov, R. Kohler, Phys. Rev. B, **52** (1995) 16369

- [54] E. A. Kondrashkina, S. A. Stepanov, R. Opitz, M. Schmidbauer, . Kohler, R. Hey, M. Wassermeier, D. V. Novikov, Phys. Rev. B, **56** (1997) 10469
- [55] J. C. S. Kools, W. Kula, D. Mauri, T. Lin, J. Appl. Phys., **85** (1999) 4466
- [56] Xuesong Jin, I. V. Shvets, J. Appl. Phys., **94** (2003) 5035